

## The ALPINE-CRISTAL-JWST Survey: The Fast Metal Enrichment of Massive Galaxies at $z \sim 5$

ANDREAS L. FAISST , LUN-JUN LIU , YOHAN DUBOIS , OMIMA OSMAN , ANDREA PALLOTTINI , LIVIA VALLINI ,  
 SEIJI FUJIMOTO , BAHRAM MOBASHER , WUJI WANG , YU-HENG LIN , RICARDO O. AMORÍN ,  
 MANUEL ARAVENA , R. J. ASSEF , ANDREW J. BATTISTI , MATTHIEU BÉTHERMIN , MÉDÉRIC BOQUIEN ,  
 PAOLO CASSATA , ELISABETE DA CUNHA , POULOMI DAM , GABRIELLA DE LUCIA , ILSE DE LOOZE ,  
 MIROSLAVA DESSAUGES-ZAVADSKY , ANDREA FERRARA , KYLE FINNER , FABIO FONTANOT , MICHELE GINOLFI ,  
 DIEGO A. GÓMEZ-ESPINOZA , CARLOTTA GRUPPIONI , NICOL GUTIÉRREZ-VERA , ALI HADI ,  
 RODRIGO HERRERA-CAMUS , MICHAELA HIRSCHMANN , EDUARDO IBAR , HANAE INAMI ,  
 JEYHAN S. KARTALTEPE , ANTON M. KOEKEMOER , MAHSA KOHANDEL , LILIAN L. LEE , YUAN LI,  
 JUAN MOLINA , AMBRA NANNI , DESIKA NARAYANAN , FRANCESCA POZZI , MONICA RELANO ,  
 MICHAEL ROMANO , DAVID B. SANDERS , JOHN D. SILVERMAN , LAURA SOMMOVIGO , JUSTIN SPILKER ,  
 AKIYOSHI TSUJITA , HANNAH ÜBLER , KEERTHI VASAN G.C. , ENRICO VERALDI , VINCENTE VILLANUEVA ,  
 LIZHI XIE AND GIANNI ZAMORANI

(AFFILIATIONS CAN BE FOUND AFTER THE REFERENCES)

### ABSTRACT

We present the stellar mass-metallicity relation (MZR) and mass-metallicity-star formation relation (“fundamental metallicity relation”; FMR) of 18 massive ( $\log(M_*/M_\odot) = 9.5 - 11$ ) main-sequence galaxies at  $z \sim 5$  from the ALPINE-CRISTAL-JWST sample. This sample complements recent studies by JWST at up to two orders of magnitude lower stellar masses. The metallicities are derived using strong optical lines, and verified by temperature-based oxygen abundance measurements for five galaxies for which faint auroral lines are detected. We find little evolution at the massive end of the MZR between  $z \sim 5$  and cosmic noon at  $z \sim 2$ , suggesting a fast metal enrichment at early times. The FMR at  $z = 5$  exhibits a  $5 \times$  larger scatter (preferentially to lower metallicities) compared the local FMR relation. This scatter can be explained by a bursty star formation and the direct build-up of metals in early galaxies as well as differences in age and outflow efficiencies. Capitalizing on all available samples, we find that the observed MZR and FMR over three orders of stellar mass is generally in good agreement with results from cosmological simulation, although some underestimate the metal enrichment at low stellar masses. This may be due to too efficient metal-rich outflows. We show that the ALPINE-CRISTAL-JWST galaxies likely joined the current FMR at  $z \sim 10$  and will evolve into massive ( $\log(M_*/M_\odot) \sim 11.4$ ) galaxies with super-solar metallicities by  $z = 0$ .

*Keywords:* Galaxy Formation (595) — Galaxy Evolution (594) — High-Redshift Galaxies (734) — Metallicity (1031) — Galaxy Structure (622) — Surveys (1671)

### 1. INTRODUCTION

Metallicity, the relative abundance of heavy elements to hydrogen, is a fundamental observable in studying the evolution of galaxies (B. M. Tinsley 1980; B. E. J. Pagel 1997; R. Maiolino & F. Mannucci 2019). Its role, to constrain the mass assembly of galaxies and the feedback process due to infall and outflow of gas, is widely used to study the chemical enrichment of galaxies. The stellar

mass vs. metallicity relation (MZR) of galaxies observed in the local universe shows the tight correlation of gas-phase metallicity increasing with the stellar mass (C. A. Tremonti et al. 2004; F. Mannucci et al. 2010; D. A. Berg et al. 2012; B. H. Andrews & P. Martini 2013; S. F. Sánchez et al. 2017; M. Curti et al. 2020). Advances in near-infrared (near-IR) spectroscopy have allowed measurements of rest-frame optical line ratio diagnostics of the metallicity of galaxies at higher redshifts. Using statistically large samples, independent studies have shown that, in general, the metal abundance at a given stel-

lar mass decreases with increasing redshift (R. Maiolino et al. 2008; D. Kashino et al. 2017; R. Maiolino & F. Mannucci 2019; R. L. Sanders et al. 2021; C. Papovich et al. 2022; A. L. Strom et al. 2022). The MOSDEF (M. Kriek et al. 2015) and KBSS (G. C. Rudie et al. 2012; C. C. Steidel et al. 2014) surveys performed extensive observations of the MZR to  $z \sim 3$ , confirming the evolution of this relation with look-back time (R. L. Sanders et al. 2018; A. L. Strom et al. 2017). The evolution and scatter in the mass-metallicity relation with redshift has strong implications towards the formation and subsequent metal enrichment of galaxies and the process of stellar evolution at earlier times.

Observations by the James Webb Space Telescope (JWST) have now given access to rest-frame optical diagnostic lines at the reionization epoch ( $z \sim 5 - 7$ ), allowing the observation of the MZR to the highest redshifts (K. Nakajima et al. 2023; M. Curti et al. 2024; A. Marszewski et al. 2024; T. Morishita et al. 2024; L. E. Rowland et al. 2025; A. Sarkar et al. 2025). This enables the study of the metal enrichment process undergone by pristine gas and the infall process in the inter-stellar medium (ISM) of early galaxies.

A serious problem in such studies was the lack of reliable calibration for metallicity measurements at high redshifts. Previous studies assumed local calibration with no significant evolution with cosmic time. This assumption directly affect the reliability of the mass-metallicity relation at  $z > 3$ . In a recent study, R. L. Sanders et al. (2024) performed a calibration between rest-frame optical line ratios and metallicities in the redshift range  $z \sim 2 - 9$  using a method based on the electron temperature ( $T_e$ ) measurement. This technique utilizes optical emission line ratios involving faint auroral lines, using transitions resulting from different upper energy levels (e.g.,  $[\text{O III}]_{4363}/[\text{O III}]_{5007}$  or  $[\text{O II}]_{7322,7332}/[\text{O II}]_{3727}$  ratios). The estimated  $T_e$  can then be used to convert dust-corrected flux ratios of ionic Oxygen lines to Hydrogen recombination lines (e.g.,  $[\text{O III}]/\text{H}\beta$  and  $[\text{O II}]/\text{H}\beta$ )<sup>54</sup> into O/H abundance ratios to construct metallicity calibration by fitting functional forms to the relation between different line ratios and O/H (M. Pettini & B. E. J. Pagel 2004; T. Nagao et al. 2006; R. Maiolino et al. 2008; M. Curti et al. 2020). This calibration procedure needs measurement of various rest-frame optical lines –  $[\text{O III}]_{4363}$ ,  $[\text{O III}]$ ,  $[\text{O II}]$ ,  $\text{H}\beta$ ,  $[\text{O II}]_{7322,7332}$  – of galaxies at high redshifts. Before JWST, it has therefore been difficult to implement this technique at high redshifts due to inaccessibility of

rest-frame optical lines and the faintness of such auroral lines. Now, all of these lines are accessible up to  $z \sim 6$  simultaneously, hence allowing a consistent metallicity measurement across the past 12 billion years.

Extending the dimensionality of the MZR by the star formation rate (SFR) led to the recognition of the fundamental metallicity relation (FMR) at low redshifts (e.g., S. L. Ellison et al. 2008; F. Mannucci et al. 2010) which was soon explained by (semi-) analytical models (e.g., R. Davé et al. 2012; P. Dayal et al. 2013; S. J. Lilly et al. 2013; R. Feldmann 2015; G. De Lucia et al. 2020). While this relation is now well established out to  $z \sim 3$  (e.g., E. Pérez-Montero et al. 2013; C. C. Steidel et al. 2014; E. Wuyts et al. 2014; K. Yabe et al. 2014; H. J. Zahid et al. 2014b,a; S. Salim et al. 2015; R. L. Sanders et al. 2015; Y. Guo et al. 2016; M. Onodera et al. 2016; D. Kashino et al. 2017; F. Cullen et al. 2019; R. L. Sanders et al. 2021; A. Henry et al. 2021; M. W. Topping et al. 2021; N. A. Korhonen Cuestas et al. 2025), only recently with JWST has it been measured at higher redshifts. These data, importantly only focusing on low-mass galaxies, suggest an evolution of the FMR compared to the local relation (M. Curti et al. 2024).

Current JWST observations referenced above have derived the MZR at stellar masses of  $\log(M_\star/M_\odot) \lesssim 9.5$  at high redshifts. The relation (and its evolution) for more massive galaxies in the early Universe are still unknown. This is mainly because such galaxies are rare and not covered by deep pencil-beam surveys (for example a  $5 \times 10^{10} M_\odot$  galaxy is ten times rarer than a  $10^9 M_\odot$  galaxy, M. Shuntov et al. 2025). Similarly, the question of a possible evolution of the FMR across the full mass range from  $10^7 - 10^{11} M_\odot$  at high redshifts is not answered. Tracing the MZR and FMR, thus the metal enrichment, in massive galaxies is an important tracer of galaxy growth and, in relation to lower stellar masses, holds valuable information on the overall evolution of galaxies.

In this work, we present constraints on the MZR and FMR at  $z \sim 5$  from galaxies of the ALPINE-CRISTAL-JWST survey (A. Faisst et al. 2025, submitted; S. Fujimoto et al. 2025, in prep). This survey provides JWST/NIRSpec IFU observations for a sample of 18 main-sequence galaxies at the end of the epoch of reionization (EoR) at  $z = 4 - 6$ . Notably, all galaxies also have ALMA observations of  $[\text{C II}]_{158 \mu\text{m}}$  and far-IR continuum at comparable resolution to JWST spectroscopy to jointly study the stars, gas, and dust at this epoch. The galaxies are massive at  $\log(M_\star/M_\odot) > 9.5$ , thus complement the samples at lower stellar masses observed by other JWST surveys. We investigate their scatter on the MZR and their location on the FMR in relation to

<sup>54</sup> In the following, we define  $[\text{O III}] \equiv [\text{O III}]_{5007}$  and  $[\text{O II}] \equiv [\text{O II}]_{3727+3730}$ .

**Table 1.** Summary of physical properties of the ALPINE-CRISTAL-JWST galaxy sample.

Name	$z_{\text{opt}}$	$M_{*}^a$ ( $10^9 M_{\odot}$ )	SFR <sup>b</sup> ( $M_{\odot} \text{yr}^{-1}$ )	Age <sup>c</sup> (Myr)	12 + log(O/H) (strong line)	12 + log(O/H) ( $T_e$ -based)	T(O <sup>+</sup> ) ( $\times 10^4 \text{ K}$ )	T(O <sup>++</sup> ) ( $\times 10^4 \text{ K}$ )	$n_e$ (cm <sup>-3</sup> )
DC-417567	5.666	$10.0^{+0.3}_{-0.3}$	$72^{+42}_{-27}$	$105^{+100}_{-56}$	$8.04^{+0.02}_{-0.02}$	$7.96^{+0.28}_{-0.14}$	$15^{+17}_{-4}$	$16^{+2}_{-2}$	$2268^{+2636}_{-912}$
DC-494763	5.233	$9.5^{+0.4}_{-0.4}$	$28^{+36}_{-16}$	$175^{+352}_{-119}$	$8.29^{+0.02}_{-0.02}$	—	—	$15^{+5}_{-3}$	—
DC-519281	5.575	$9.8^{+0.4}_{-0.4}$	$32^{+35}_{-17}$	$324^{+331}_{-194}$	$7.99^{+0.08}_{-0.08}$	—	—	—	$637^{+1430}_{-321}$
DC-536534	5.689	$10.4^{+0.3}_{-0.3}$	$62^{+64}_{-31}$	$456^{+275}_{-224}$	$8.10^{+0.04}_{-0.05}$	—	$14^{+6}_{-3}$	$18^{+2}_{-3}$	—
DC-630594	4.440	$9.7^{+0.3}_{-0.3}$	$37^{+39}_{-19}$	$186^{+227}_{-88}$	$8.40^{+0.04}_{-0.04}$	$7.99^{+0.29}_{-0.19}$	$17^{+8}_{-3}$	$15^{+3}_{-3}$	$185^{+246}_{-116}$
DC-683613	5.541	$10.2^{+0.3}_{-0.3}$	$68^{+67}_{-34}$	$274^{+271}_{-159}$	$8.49^{+0.03}_{-0.05}$	—	$19^{+14}_{-4}$	—	$547^{+411}_{-262}$
DC-709575	4.412	$9.5^{+0.4}_{-0.4}$	$28^{+39}_{-16}$	$190^{+302}_{-95}$	$8.27^{+0.02}_{-0.03}$	$8.01^{+0.34}_{-0.20}$	$13^{+4}_{-3}$	$18^{+3}_{-2}$	$484^{+685}_{-238}$
DC-742174	5.636	$9.5^{+0.4}_{-0.4}$	$15^{+16}_{-8}$	$354^{+338}_{-215}$	$7.84^{+0.05}_{-0.05}$	—	—	—	—
DC-842313	4.552	$10.6^{+0.5}_{-0.5}$	$204^{+918}_{-167}$	$394^{+250}_{-221}$	$8.48^{+0.03}_{-0.05}$	$8.49^{+0.37}_{-0.27}$	$11^{+3}_{-2}$	$13^{+9}_{-0}$	$154^{+122}_{-87}$
DC-848185	5.294	$10.3^{+0.3}_{-0.3}$	$178^{+290}_{-110}$	$98^{+52}_{-48}$	$8.28^{+0.02}_{-0.03}$	$8.06^{+0.22}_{-0.22}$	$15^{+3}_{-3}$	$14^{+4}_{-2}$	$388^{+153}_{-147}$
DC-873321	5.154	$10.0^{+0.3}_{-0.3}$	$78^{+64}_{-35}$	$112^{+84}_{-63}$	$8.11^{+0.06}_{-0.07}$	—	$15^{+9}_{-3}$	—	$613^{+307}_{-291}$
DC-873756	4.545	$10.5^{+0.1}_{-0.1}$	$115^{+76}_{-46}$	$550^{+317}_{-169}$	$8.68^{+0.58}_{-0.88}$	—	—	—	—
VC-5100541407	4.563	$10.1^{+0.3}_{-0.3}$	$42^{+50}_{-23}$	$400^{+427}_{-239}$	$8.21^{+0.24}_{-0.40}$	—	—	—	—
VC-5100822662	4.520	$10.2^{+0.3}_{-0.3}$	$78^{+48}_{-30}$	$237^{+196}_{-122}$	$8.33^{+0.04}_{-0.04}$	—	—	$15^{+4}_{-3}$	$299^{+174}_{-194}$
VC-5100994794	4.580	$9.6^{+0.3}_{-0.3}$	$32^{+51}_{-20}$	$193^{+252}_{-95}$	$8.41^{+0.04}_{-0.05}$	—	$15^{+6}_{-3}$	—	$1153^{+289}_{-411}$
VC-5101218326	4.573	$10.9^{+0.3}_{-0.3}$	$562^{+534}_{-274}$	$646^{+97}_{-275}$	$8.36^{+0.34}_{-0.30}$	—	—	—	—
VC-5101244930	4.581	$9.7^{+0.3}_{-0.3}$	$28^{+20}_{-12}$	$183^{+365}_{-88}$	$8.24^{+0.10}_{-0.13}$	—	$17^{+15}_{-4}$	—	—
VC-5110377875	4.550	$10.2^{+0.2}_{-0.2}$	$99^{+75}_{-43}$	$161^{+127}_{-108}$	$8.41^{+0.08}_{-0.09}$	—	$13^{+13}_{-3}$	—	$924^{+767}_{-525}$

NOTE—<sup>a</sup> Stellar masses are derived in [I. Mitsuhashi et al. \(2024\)](#).

<sup>b</sup> SFRs represent the total UV+FIR luminosities derived in [A. Faisst et al. \(2025, submitted\)](#).

<sup>c</sup> Ages (light-weighted) are derived in [A. L. Faisst et al. \(2020\)](#).

theoretical models to characterize the fast build-up of metals at these early times.

This paper is organized as follows: In Section 2, we describe the sample and outline the measurement of the metal abundances (with more details in Appendix A). In Section 3, we present the observed MZR and FMR at  $z \sim 5$ , which we then study in the light of a simple analytical model and cosmological simulations in Section 4. Throughout this work, we assume a  $\Lambda$ CDM cosmology with  $H_0 = 70 \text{ km s}^{-1} \text{ Mpc}^{-1}$ ,  $\Omega_{\Lambda} = 0.7$ , and  $\Omega_m = 0.3$  and magnitudes are given in the AB system ([J. B. Oke 1974](#)). We use a Chabrier initial mass function (IMF; [G. Chabrier 2003](#)) calibration for stellar masses and SFRs.

## 2. DATA & MEASUREMENTS

### 2.1. The ALPINE-CRISTAL-JWST Sample

This work is based on the 18 of the ALPINE-CRISTAL-JWST survey. The survey, including science goals and basic measurements, is described in its entirety in [A. Faisst et al. \(2025, submitted\)](#). The JWST/NIRSpec IFU data reduction and spatially resolved metallicity measurements are described in [S. Fujimoto et al. \(2025, in prep\)](#). Here, we give a brief overview of the sample and the survey.

The ALPINE-CRISTAL-JWST survey targeted 18 main-sequence galaxies at  $4.4 < z < 5.9$  ( $\langle z \rangle \sim 5$ ) from the ALMA-ALPINE program ( $[\text{C II}]_{158 \mu\text{m}}$  and  $158 \mu\text{m}$  dust continuum observations at  $0.7''$  spatial resolution; [O. Le Fèvre et al. 2020](#); [M. Béthermin et al. 2020](#); [A. L. Faisst et al. 2020](#)) at  $\log(M_{*}/M_{\odot}) \sim 9.5 - 11.0$  and  $\text{SFR} \sim 10 - 700 M_{\odot} \text{ yr}^{-1}$  with rest-frame optical JWST/NIRSpec IFU observations (#3045; PI: Faisst) at  $0.15''$  spatial resolution in G235M/F170LP and G395M/F290LP ( $R \sim 1000$ ). As part of the selection process, all galaxies have HST rest-frame ultraviolet (UV) imaging, JWST/NIRCam rest-frame optical imaging (COSMOS-Web program; [C. M. Casey et al. 2022](#)), and additional higher resolution ALMA observations of the  $[\text{C II}]_{158 \mu\text{m}}$  line and the  $158 \mu\text{m}$  dust continuum at  $0.3''$  spatial resolution from the ALMA-CRISTAL survey ([R. Herrera-Camus et al. 2025](#)). All galaxies reside in the COSMOS field ([N. Scoville et al. 2007](#); [A. M. Koekemoer et al. 2007](#)), which provides a wealth of ancillary data.

Although none of our targets can be unambiguously defined as AGN based on the BTP diagram ([J. A. Baldwin et al. 1981](#)), one of them (*DC-873756*) shows strong  $[\text{N II}]$  emission, making it a potential BPT candidate AGN. In addition, other six targets (*DC-417567*,

*DC-519281, DC-536534, DC-683613, DC-848185, and DC-873321* are potential type 1 AGN due to broad ( $> 500$  km/s)  $\text{H}\alpha$  emission (W. Ren et al. 2025, submitted).

Some physical parameters are summarized in Table 1 (more can be found in A. Faisst et al. 2025, submitted). The stellar masses adopted in this work are derived in I. Mitsuhashi et al. (2024) using the CIGALE code (M. Boquien et al. 2019; D. Burgarella et al. 2005). The SFRs are derived from the total UV+far-IR emission (A. Faisst et al. 2025, submitted). The galaxy ages (light weighted) are taken from A. L. Faisst et al. (2020) and are derived using LePhare (S. Arnouts et al. 1999; O. Ilbert et al. 2006). Four galaxies are not far-IR detected and we use the SED-fitting results from I. Mitsuhashi et al. (2024) to measure their SFR.  $\text{H}\alpha$ -based SFRs extinction-corrected with Balmer decrement are derived using the J. Kennicutt (1998) relation (converted to a G. Chabrier (2003) IMF).

The ALPINE-CRISTAL-JWST survey provides the best-studied  $z \sim 5$  main-sequence galaxy sample at  $\log(M/M_\odot) = 9.5 - 11.0$  at  $1 - 2$  kpc resolution to date. It is a benchmark in the study of galaxy evolution in the post-EoR era — the connection between primordial galaxy formation in the EoR and mature galaxy evolution at cosmic noon.

## 2.2. Metallicity Measurement

From the new JWST/NIRSpec spectroscopy, we measured spatially integrated oxygen abundances (“metallicity”, defined as  $Z \equiv 12 + \log(\text{O/H})$ ) of the 18 galaxies using strong optical emission lines with applied  $T_e$  calibration from R. L. Sanders et al. (2024). These strong lines are detected for all individual galaxies. The metallicity measurements are detailed in A. Faisst et al. (2025, submitted) and summarized in Table 1 and in the following we give an overview. In Appendix A, we additionally compare different strong-line metallicity calibrators as well as compare these measurement to direct metallicity measurements from fainter auroral lines for a subsample of five galaxies.

The measurement of the strong-line metallicities is based on the dust-corrected optical lines fluxes of  $[\text{O II}]$ ,  $\text{H}\beta$ , and  $[\text{O III}]$  to derive oxygen abundances (see review on metallicity measurements in L. J. Kewley et al. 2019). All emission lines are extracted from the spectral cubes in a mask defined by the region of the  $3\sigma$  JWST/NIRCam rest-frame optical continuum flux (*i.e.* tracing the stellar mass). But note the results do not depend significantly on the exact spatial outline. We do not use  $\text{H}\alpha$  and  $[\text{N II}]$  in the case of contamination by an AGN (W. Ren et al. 2025, submitted) and the blend-

**Table 2.** Fit to mass–metallicity relation (MZR; Figure 1) using all current data at  $z = 4 - 6$ . Functional form:  $12 + \log(\text{O/H}) = B (\log(M_\star/M_\odot) - \log(M_0))^2 + A$

$\log(M_0)$	A	B
$14.95 \pm 5.98$	$8.75 \pm 0.75$	$-0.02 \pm 0.02$

NOTE—Data included from: This work (ALPINE-CRISTAL-JWST; A. Faisst et al. 2025, submitted); K. Nakajima et al. (2023); T. Morishita et al. (2024); M. Curti et al. (2023); A. Sarkar et al. (2025); K. E. Heintz et al. (2025)

ing of the two lines in the medium resolution spectra. Dust correction was applied via the Balmer decrement ( $\text{H}\alpha/\text{H}\beta$ ) assuming case B recombination. Due to the coverage with both the G235M and G395M grating, the same lines could be used for all galaxies in the sample. We use the parameterization and calibration by R. L. Sanders et al. (2024), which we found to lead to consistent with parameterization by R. Maiolino et al. (2008) and M. Hirschmann et al. (2023) (Figure A.1, Appendix A).

The strong-line metallicity measurements were also compared to direct  $T_e$ -based measurements derived from fainter auroral lines ( $[\text{O III}]_{4363}$  and  $[\text{O III}]_{7322,7332}$ ) for a subset of five galaxies. For these galaxies, we find consistent metallicity measurement from the strong-line method an the  $T_e$  method (see Appendix A for details).

As mentioned previously, six of the ALPINE-CRISTAL-JWST galaxies are potential type 1 AGN candidates. However, as they do not seem to exhibit unusual line ratios typical for BPT AGN, we do not think that their possible AGN activity has a significant effect on the metallicity measurement.

## 3. THE MASS-Z-SFR RELATION OF MASSIVE MAIN-SEQUENCE GALAXIES AT $Z \sim 5$

The build-up of metals directly relates to the build-up of stellar mass over the lifetime of galaxies. However, second-order deviations from such a relation provide important insights into changes of metal production due to different processes such as star formation efficiency, outflows, inflows, and other physical events (e.g., supernovae or changes in the IMF). With JWST, it has now become possible to constrain the metal content of galaxies close to the EoR at  $z = 6$ . So far, JWST provided such measurements for low-mass systems, generally well below  $\log(M_\star/M_\odot) = 9.5$ . The ALPINE-CRISTAL-JWST survey provides a sample of more massive  $z \sim 5$  galaxies that complements these other measurements and extends the relation between stellar mass, SFR, and metallicity to the massive end to  $\log(M_\star/M_\odot) = 11$  at  $z \sim 5$ .

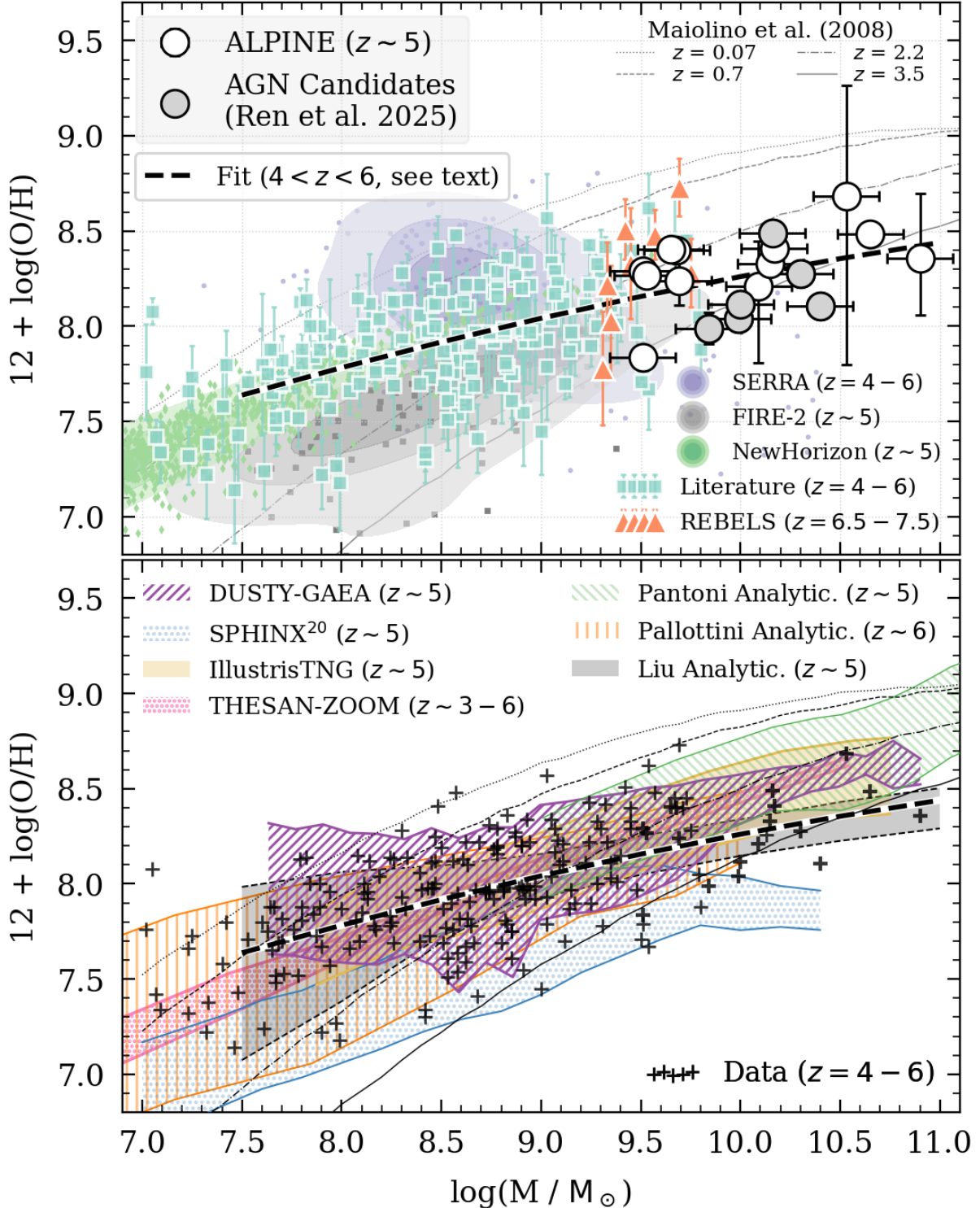


**Figure 1.** The stellar mass vs. metallicity relation (MZR) at  $z \sim 5$ . *Top:* The observed MZR of the  $z \sim 5$  ALPINE-CRISTAL-JWST sample (large open circles; six type 1 broad-line AGN candidates identified by (W. Ren et al. 2025, submitted) are indicated in gray). Other observations with JWST at  $z = 4 - 6$  (turquoise squares; K. Nakajima et al. 2023; T. Morishita et al. 2024; M. Curti et al. 2024; A. Sarkar et al. 2025; K. E. Heintz et al. 2025) and at  $z = 6.5 - 7.5$  (gold triangles, REBELS-IFU; L. E. Rowland et al. 2025) are also shown. The thick dashed line shows a fit to all  $z = 4 - 6$  data (see Equation 1 and Table 2). The contours show results from the cosmological simulations SERRA (blue; A. Pallottini et al. 2022), FIRE-2 (gray; X. Ma et al. 2016; A. Marszewski et al. 2024), and NEWHORIZON (green; Y. Dubois et al. 2021). Dotted, dashed, dot-dashed, and thin solid line shows the MZR parameterizations by R. Maiolino et al. (2008) at  $z < 3.5$ . *Bottom:* The same observational data (black crosses) compared to other cosmological simulations; ILLUSTRISTNG (gold shaded at  $z = 4 - 6$ ; M. Hirschmann et al. 2023), SPHINX<sup>20</sup> (blue dot-hatched; J. Rosdahl et al. 2018, 2022; H. Katz et al. 2023), DUSTY-GAEA (purple forward line-hatched; O. Osman et al. 2025, in prep), and THESAN-ZOOM (pink dot-hatched; R. Kannan et al. 2025). In addition, we show other analytical models from L. Panti (2019) (green backward-hatched), A. Pallottini et al. (2025) (orange vertical-hatched), and L.-J. Liu et al. (2024) (gray shaded).

### 3.1. The Mass-Metallicity Relation (MZR)

The upper panel of Figure 1 shows the resulting MZR for the ALPINE-CRISTAL-JWST sample (large circles and type 1 AGN candidates indicated in gray). The measured abundances range from  $7.7 - 8.5$  in  $12 + \log(\text{O/H})$ , corresponding to  $10 - 70\%$  of solar metallicity<sup>55</sup>. We compare these observations to measurements of lower-mass galaxies from the literature at  $z = 4 - 6$  (including K. Nakajima et al. 2023; T. Morishita et al. 2024; M. Curti et al. 2024; A. Sarkar et al. 2025; K. E. Heintz et al. 2025) and  $z = 6.5 - 7.5$  (REBELS-IFU; L. E. Rowland et al. 2025). These measurements use calibrations consistent with our work and we therefore do not expect significant systematics. Also shown are the mass-metallicity parameterizations at lower redshifts from R. Maiolino et al. (2008). The comparison to cosmological simulations and analytical models will be discussed in Section 4.3.

As expected, we find that the ALPINE-CRISTAL-JWST galaxies lie at the high-mass end of the distribution, ideally complementing existing studies at lower masses. Their metal abundances compare reasonably with the abundances of these lower-mass galaxies; they are generally about 0.5 dex more metal enriched compared to galaxies at  $\log(M_*/M_\odot) < 9$ . However, it is noticeable that there is no significant evolution (meaning increase) in the metal abundances at a given stellar mass between galaxies in the EoR ( $z = 6 - 7.5$ ), post EoR ( $z = 4 - 6$ ), and at cosmic noon ( $z = 2$ , cf. R. Maiolino et al. 2008 tracks in Figure 1) even though galaxies evolve significantly in mass and structure during these 3 Gyrs. In fact, the average metal abundance of the ALPINE-CRISTAL-JWST sample at  $z \sim 5$  is statistically similar to galaxies at  $z \sim 2 - 3$  at the same stellar masses (c.f. C. C. Steidel et al. 2014; R. L. Sanders et al. 2015). We discuss possible reasons for this and the weak evolution of metal abundances in Section 4.

The thick black dashed line in Figure 1 shows a fit using the `scipy.optimize` Python package to all available data at  $z = 4 - 6$  and  $\log(M_*/M_\odot) = 7.5 - 11.0$  including the ALPINE-CRISTAL-JWST sample:<sup>56</sup>

$$12 + \log(\text{O/H}) = B (\log(M_*/M_\odot) - \log(M_0))^2 + A, \quad (1)$$

with best-fit parameters given in Table 2.

<sup>55</sup> We assume here a solar value of  $12 + \log(\text{O/H}) = 8.69$  (C. Allende Prieto et al. 2001), however, note that this value could be higher (M. Bergemann et al. 2021).

<sup>56</sup> We adopt here a common functional form as in R. Maiolino et al. (2008).

### 3.2. The Fundamental Metallicity Relation (FMR)

In addition to the MZR it is known that galaxies also follow a similar relation between stellar mass, metallicity, and SFR (the so-called “fundamental metallicity relation” or FMR, e.g., S. L. Ellison et al. 2008; M. A. Lara-López et al. 2010; F. Mannucci et al. 2010; B. H. Andrews & P. Martini 2013; M. Curti et al. 2020). This fundamental relation, specifically the anti-correlation between metallicity and SFR, has also been identified in analytical models and numerical simulations (R. Davé et al. 2012; P. Dayal et al. 2013; S. J. Lilly et al. 2013; R. Feldmann 2015; G. De Lucia et al. 2020). They support the idea of reducing the metal abundances in the ISM due to the infall of pristine/metal-poor gas, which is related to an increased star formation. This three-dimensional relation has been well studied out to  $z = 2 - 3$  (e.g., C. C. Steidel et al. 2014; E. Wuyts et al. 2014; K. Yabe et al. 2014; H. J. Zahid et al. 2014b,a; S. Salim et al. 2015; R. L. Sanders et al. 2015; Y. Guo et al. 2016; M. Onodera et al. 2016; D. Kashino et al. 2017; F. Cullen et al. 2019; R. L. Sanders et al. 2021; A. Henry et al. 2021; M. W. Topping et al. 2021; N. A. Korhonen Cuestas et al. 2025), however, no comprehensive studies at higher redshifts cover the full mass range of galaxies have been undertaken. Here we combine the massive ALPINE-CRISTAL-JWST sample with measurements at lower masses from the literature to test for the first time the universality of a FMR at  $z \sim 5$ .

The left panel in Figure 2 shows that the FMR is already in place at  $z \sim 5$ . Specifically, this figure shows our new measurements from the ALPINE-CRISTAL-JWST sample at  $z \sim 5$  together with data points from SDSS at  $z \sim 0$  (K. N. Abazajian et al. 2009; S. Alam et al. 2015) and FMOS at  $z \sim 1.6$  (J. D. Silverman et al. 2015; D. Kashino et al. 2017). The lines show the common *equilibrium* gas-regulator (“bathtub”) models from S. J. Lilly et al. (2013) (see also C. Maier et al. 2014; A. Dekel & N. Mandelker 2014; R. Feldmann 2015; M. Onodera et al. 2016) calibrated by D. Kashino et al. (2017) to the  $z = 0$  data from SDSS. In this model, the equilibrium metallicity depends on stellar mass and SFR as follows:

$$Z_{\text{eq}} = Z_{\text{in}} + \frac{y}{1 + \lambda(1 - R)^{-1} + \epsilon_{\text{out}}^{-1} \left( (1 + \beta - b) \times \frac{\text{SFR}}{M_*} - 0.15 \right)}, \quad (2)$$

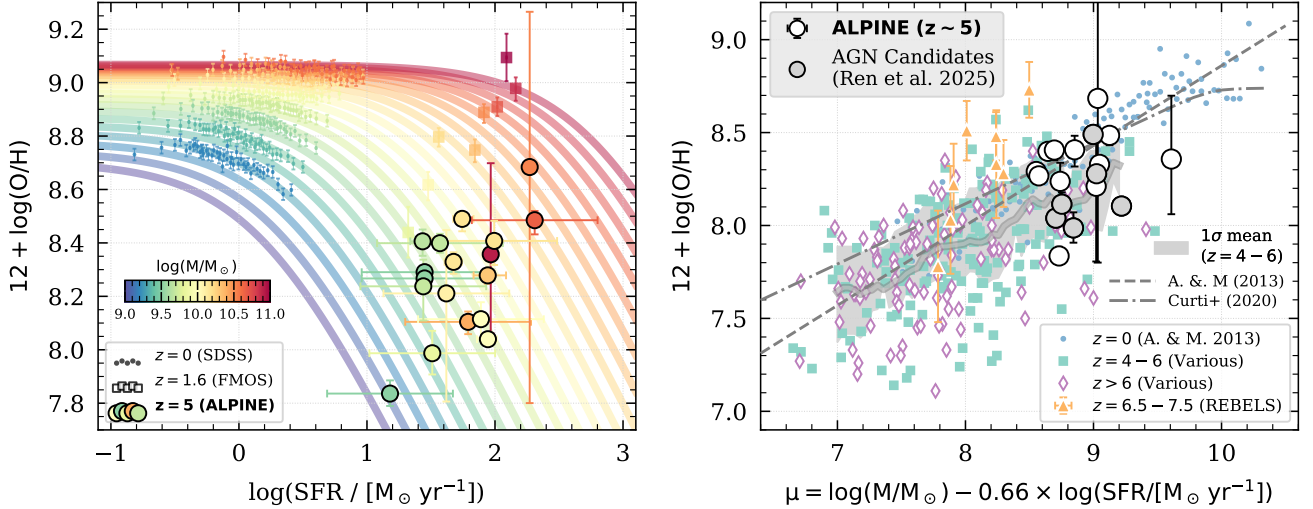


**Figure 2.** The stellar mass, metallicity, and SFR relation (“fundamental metallicity relation”, FMR). *Left:* Data are shown at  $z = 0$  from SDSS (small circles), at  $z \sim 2$  from the FMOS survey (large squares; J. D. Silverman et al. 2015; D. Kashino et al. 2017), and from the ALPINE-CRISTAL-JWST survey at  $z \sim 5$  (large circles; this work). The data are compared to an equilibrium gas-regulator model (see Equation 2) from S. J. Lilly et al. (2013) (see also C. Maier et al. 2014; M. Onodera et al. 2016), calibrated by D. Kashino et al. (2017) to the SDSS  $z = 0$  measurements (colored lines). The symbols and lines are color-coded by stellar mass on the same scale. *Right:* The collapsed FMR assuming  $\mu_0 = 0.66$  (B. H. Andrews & P. Martini 2013). The ALPINE-CRISTAL-JWST sample at  $z \sim 5$  is shown as large circles (type 1 AGN candidates from W. Ren et al. 2025, submitted indicated in gray). Other literature data are shown at  $z = 4 - 6$  and  $z > 6$  (K. Nakajima et al. 2023; M. Curti et al. 2024; T. Morishita et al. 2024; A. Sarkar et al. 2025; K. E. Heintz et al. 2025) as well as from the REBELS-IFU survey (L. E. Rowland et al. 2025). The small blue points are data at  $z = 0$  (B. H. Andrews & P. Martini 2013) with the corresponding fit shown as dashed gray line. The dot-dashed gray line shows the  $z = 0$  parameterization by M. Curti et al. (2020). The gray band shows the  $1\sigma$  percentiles of the literature and ALPINE-CRISTAL-JWST data at  $z = 4 - 6$ .

where  $Z_{\text{in}}$  is the metallicity of the inflowing gas,  $y$  is the metal yield<sup>57</sup>,  $R$  is the fraction of mass returned to the ISM,  $\lambda = \lambda_0 \times \left(\frac{M_*}{10^{10} M_\odot}\right)^a$  is the mass-loading factor,  $\epsilon_{\text{out}} = \epsilon_{\text{out},0} \times \left(\frac{M_*}{10^{10} M_\odot}\right)^b$  is the star formation efficiency (e.g., 1/Gyr), and  $\beta = -0.25$  is the slope of the relation between stellar mass and specific SFR. For consistency, we assume here the same values as in D. Kashino et al. (2013);  $Z_{\text{in}} = 0$ ,  $\log(y) = 9.09$ ,  $R = 0.27$ ,  $(\lambda_0, a) = (0.38, -0.61)$ , and  $(\epsilon_{\text{out},0}, b) = (0.53, 0.48)$ . For the derivation of the subtraction  $-0.15$ , see equation 40 in S. J. Lilly et al. (2013). Both our analytical model and data points are color-coded by stellar mass in the same color scale. The colors of the ALPINE-CRISTAL-JWST galaxies and the equilibrium model curves (notably calibrated to the  $z = 0$  sample) agree well, suggesting that galaxies at  $z \sim 5$  follow a similar FMR as local galaxies.

The right panel in Figure 2 visualizes the above in more detail by showing an angled slice through the FMR by defining  $\mu \equiv \log(M_\star) - \mu_0 \times \log(\text{SFR})$  where  $\mu_0 = 0.66$

based on a fit to galaxies at  $z = 0$  (B. H. Andrews & P. Martini 2013). The ALPINE-CRISTAL-JWST galaxies are shown as large symbols together with literature data in two redshift bins at  $z = 4 - 6$  and  $z > 6$  (K. Nakajima et al. 2023; M. Curti et al. 2024; T. Morishita et al. 2024; A. Sarkar et al. 2025; K. E. Heintz et al. 2025; L. E. Rowland et al. 2025). Note that we find a tentative trend of type 1 AGN candidate host galaxies to show a lower metallicity, however this claim needs to be confirmed with larger samples.

Of interest is the comparison to the local FMR parameterized as  $12 + \log(\text{O/H}) = 0.43\mu + 4.56$  by B. H. Andrews & P. Martini (2013) (dashed line, right panel of Figure 2). To first order galaxies at  $z = 4 - 6$  follow this local relation well but to second order the data suggest a scatter towards lower metallicity at a given  $\mu$ . This indicates an evolving FMR compared to  $z = 0$ . This finding is in agreement with a recent study by M. Curti et al. (2024), although they find a larger offset and scatter, hence a stronger evolution of the FMR. This is due to a different calibration of the local FMR – indeed, the evolution is stronger if the parameterization by M. Curti

<sup>57</sup> Here, the yield is non-dimensional and defined as the mass of metals returned to the ISM per unit mass that is locked up in long-lived stars, *i.e.*  $(1 - R)$  times the mass of stars formed; see S. J. Lilly et al. (2013).

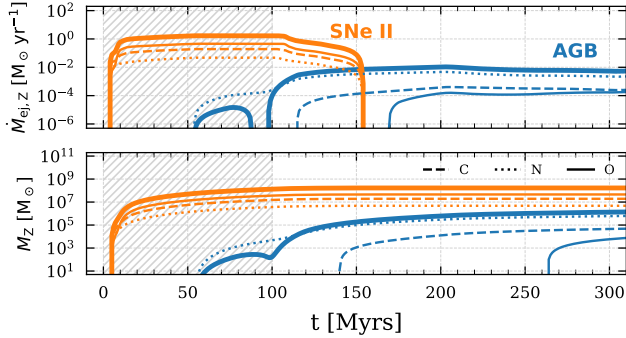


**Figure 3.** Illustration of the metal build-up from our simple analytical model. We assume a starburst forming  $5 \times 10^9 \text{ M}_\odot$  within 100 Myr at a rate of  $50 \text{ M}_\odot \text{yr}^{-1}$  (hatched area). *Top:* Instantaneous metal ejection rate ( $\dot{M}_{ej,Z}$ ) over time from type II SNe and AGB stars for carbon (dashed), nitrogen (dotted), oxygen (solid), and their sum (thick solid). *Bottom:* Cumulative ejected metal mass over time.

et al. (2020) (dot-dashed line)<sup>58</sup> is used. However, the result at high stellar masses (also showing a downward scatter in the FMR) is independent on the assumption of the  $z = 0$  FMR relation.

#### 4. DISCUSSION

In the previous section, we have reported on the MZR (Figure 1) as well as the FMR (Figure 2) at  $z \sim 5$  for massive galaxies in the ALPINE-CRISTAL-JWST sample. The data show that there is little evolution in the metal abundance from the EoR to cosmic noon at a given stellar mass (Figure 1) and in addition galaxies at  $z \sim 5$  lie to first order on the same FMR as galaxies at  $z = 0$  and  $z \sim 1.6$  (Figure 2). This indicates a fast build-up of metals at early times and subsequent steady main-sequence enrichment to the local universe. However, to second order there are differences to the average low-redshift galaxy population: there is a significant scatter towards low metallicities at a given stellar mass compared to the local relations. In the following, we investigate the MZR and FMR scatter and compare the observations to a simple analytical model and cosmological simulations.

##### 4.1. The build-up of metals in the view of a simple analytical model

We start by implementing a simple analytical model, whose details can be reviewed in R. Feldmann (2015) as well as the related papers (S. J. Lilly et al. 2013; H. J. Zahid et al. 2014a; R. Davé et al. 2012). In brief,

<sup>58</sup> Note that M. Curti et al. (2020) derives a  $\mu_0 = 0.65$  for the high ssFR SDSS sample, which is in agreement with the value adopted here (0.66) derived by B. H. Andrews & P. Martini (2013). For consistency, we use 0.66 in this work.

galaxies are treated as semi-closed boxes allowing the inflow and outflow of gas, thereby following simple continuity equations. The star formation is regulated by a star formation efficiency (or depletion time), and the metal and dust evolution is coupled to star formation by empirical yields and modified by the inflow and outflow (e.g., through feedback from stellar winds and Supernovae) of gas. Thus the evolution of a galaxy through cosmic time is overall described by a given gas accretion rate ( $\dot{M}_{\text{gas,in}}$ ), the metallicity of the infalling gas (given by the per-cent fraction to the ISM metal-to-gas ratio;  $r_Z$ ), outflow rate (mass-loading factor,  $\epsilon_{\text{out}} \equiv \frac{\dot{M}_{\text{out}}}{\text{SFR}}$ ), and star formation efficiency (SFE) or gas depletion time ( $t_{\text{depl}} \propto \text{SFE}^{-1}$ ). Note that these parameters may be dependent on time, stellar mass, and star formation. For our simple demonstration purpose (and to minimize the number of variables) we treat the accretion rate and depletion time as time-independent constant factors motivated by observations. However, the mass-loading factor  $\epsilon_{\text{out}}$ , which controls the slope of the mass-metallicity relation, is dependent on stellar mass and redshift as discussed below.

We derive the stellar mass, SFR, gas and dust mass empirically by running the model forward in time, thereby computing these parameters in every time step

$$\begin{aligned} M_\star(t) &= M_\star(t - \Delta t) + \dot{M}_\star(t) \Delta t, \\ \text{SFR}(t) &\equiv \dot{M}_\star(t) = \frac{M_{\text{gas}}(t)}{\langle t_{\text{depl}} \rangle}, \\ M_{\text{gas}}(t) &= M_{\text{gas}}(t - \Delta t) + \langle \dot{M}_{\text{gas,in}} \rangle \Delta t, \\ M_Z(t) &= M_Z(t - \Delta t) + \dot{M}_Z(t) \Delta t. \end{aligned} \quad (3)$$

The core of this calculation is the computation of the total metal mass ( $M_Z$ ) via the effective metal enrichment of the ISM, which can be written as

$$\begin{aligned} \dot{M}_Z(t) &= \dot{M}_{ej,Z}(t) - \zeta (1 - R) \dot{M}_\star(t) \\ &\quad - \zeta \epsilon_{\text{out}}(M_\star, t) \dot{M}_\star(t) + r_Z \zeta \dot{M}_{\text{gas,in}}, \end{aligned} \quad (4)$$

where  $\dot{M}_{ej,Z}$  is the total metal ejection rate,  $R = 0.46$  (M. R. Krumholz & A. Dekel 2012; R. Feldmann 2015), and  $\zeta \equiv \frac{M_Z(t)}{M_{\text{gas}}(t)}$  is the metal-to-gas mass ratio of the ISM. In words, the metal production rate is altered by the lock-up of metals in the stars, the outflow of metal-rich gas, and the inflow of gas (which may be metal enriched or metal poor). The oxygen abundance metallicity is then computed as  $12 + \log(\text{O/H}) = 8.69 + \log(\zeta / 0.014)$  (C. Allende Prieto et al. 2001; R. Feldmann 2015) using the calibration  $Z_\odot \sim 0.014$  (M. Asplund et al. 2009).

For deriving the mass-loading factor (which is dependent on stellar mass and redshift), we use the results from the EAGLE cosmological simulation (J. Schaye et al. 2015; R. A. Crain et al. 2015), specifically from the work by P. D. Mitchell et al. (2020, figure 3), which we parameterized analytically by a double power-law as described in Appendix B. This parameterization is consistent with the one by A. L. Muratov et al. (2015) based on the FIRE simulation (P. F. Hopkins et al. 2014).

While previous studies have assumed a constant yield for the production of metals, we adopt here more realistic metallicity ejection rates into the ISM. Specifically, we used the mass-dependent metal yields computed for Asymptotic Giant Branch (AGB) stars and type II Supernovae (SNe) from F. Dell’Agli et al. (2019) and M. Limongi & A. Chieffi (2018), respectively, to obtain the mass ejection rates ( $\dot{M}_{\text{ej},z}$ ) into the ISM for carbon, nitrogen, and oxygen as a function of time for a given star formation history (SFH) and IMF<sup>59</sup>. We include stars in the range of  $1 - 7 M_{\odot}$  for AGB yields and  $7 - 120 M_{\odot}$  for SNe II yields<sup>60</sup> and use their mass-dependent lifetimes given in L. Portinari et al. (1998). Figure 3 shows the immediate mass ejection rate into the ISM (top panel) and the cumulative total ejected metal mass (bottom panel) as a function of time based on this model. In this educational example, we assumed a simple SFH in the form of a starburst with constant SFR over  $\Delta t = 100$  Myr (hatched area) and a total produced stellar mass of  $5 \times 10^9 M_{\odot}$  (no SFR before or after burst). It is evident that type II SNe contribute the bulk of metals early on within  $\sim 150$  Myrs after the start of the burst. AGB stars (at lower masses) contribute most of the ejecta at  $> 100$  Myrs<sup>61</sup>.

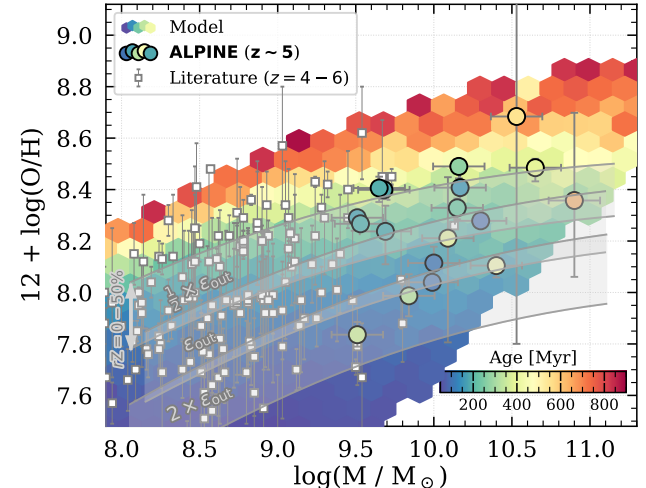
This simple analytical model successfully reproduces the observed star-forming main sequence at  $z \sim 5$  (e.g., Y. Khusanova et al. 2021) and lower redshifts, assuming reasonable average values of  $t_{\text{depl}} = 5 \times 10^8$  yr (e.g., M. Dessauges-Zavadsky et al. 2020) and accretion rates  $\dot{M}_{\text{gas,in}} = 100 M_{\odot} \text{ yr}^{-1}$  (e.g., N. Scoville et al. 2023).

Figure 4 shows the resulting MZR of our model at  $z \sim 5$  (hexagonal bins). The model output is color-

<sup>59</sup> In the end, we assume to sum of these elements to contribute to metallicity.

<sup>60</sup> Note that cores of stars more massive than  $40 M_{\odot}$  may collapse to form black holes resulting in less metal output into the ISM. However, limiting our calculation to this mass limit has a negligible impact on the following results.

<sup>61</sup> Note that carbon yields in the most massive stars can be negative as the surface chemistry of these objects is mostly determined by hot bottom burning, which destroys carbon in the envelope. This causes the drop in the total metal abundance at  $\sim 150$  Myrs after the onset of star formation.



**Figure 4.** The MZR reproduced by our analytical model at  $z \sim 5$  (see Section 4.1 for details). Model galaxies are color-coded by their age. ALPINE-CRISTAL-JWST galaxies are shown as large symbols with same color code and other literature data are shown as gray squares (see also Figure 1). Our model captures well the range of observations and visualizes the fast metal enrichment. The upper envelope of the MZR is set by maximally old model galaxies (red). The observed galaxy ages correlate well with the model ages. The three gray swaths show model track ranges for two different outflow efficiencies including the nominal mass-loading factor from P. D. Mitchell et al. (2020). Lower outflow efficiencies increase the metal content at a given stellar mass. The width of the swaths shows a range in the metallicity of the inflowing gas from metal free ( $r_z = 0$ ) to 50% ( $r_z = 0.5$ ) of the metallicity of the ISM gas.

coded by the age of the stellar population between 50 Myrs (blue) and 900 Myrs (red). The data from the ALPINE-CRISTAL-JWST sample are shown as large circles color-coded by age<sup>62</sup> on the same color scale. Other data from the literature at  $z = 4 - 6$  are shown as gray squares (same as Figure 1). This simple analytical model with realistic metal yields is able to reproduce the parameter space of observations on the MZR at  $z \sim 5$  (Figure 4). In fact, our model also reproduces the FMR. Importantly, it is also broadly consistent with most of the observed ages of the ALPINE-CRISTAL-JWST galaxies (shown at same color scale in Figure 4). We note that the measurement of ages comes with large uncertainties (factors of two or more), which could explain some of the discrepancies between the observed and model ages. Furthermore, the SED-fit ages may be younger as they capture commonly the age since the

<sup>62</sup> The ages are derived from SED fitting assuming delayed  $\tau$  models, see A. L. Faisst et al. (2020) and A. Tsujita et al. (2025, in prep.).

last significant starburst, while the ages output by our model are the times since first star formation. The upper boundary of the MZR is given in our model by the maximal age of a galaxy at  $z \sim 5$ , hence maximal cumulative metal abundance produced by our model. The model reemphasizes the fast metal build-up; metallicities of  $12 + \log(\text{O/H}) \sim 8.3$  (the median at  $3 \times 10^9 \text{ M}_\odot$ ) are reached after only 200 Myrs of star formation.

In addition, we can investigate the impact of gas inflows and the mass loading factor on the results. The three gray swaths in Figure 4 show our analytical model with three different mass-loading implementations: the nominal  $\epsilon_{\text{out}}$  as well as two adjustment;  $0.5 \times \epsilon_{\text{out}}$  and  $2 \times \epsilon_{\text{out}}$ . (Note that this is equivalent to  $\epsilon_{\text{SN}} = 0.5$  and 2 in [A. Pallottini et al. 2025](#).) The width of the swaths shows a range of relative metal enrichment of the infalling gas from pristine (0%) to 50% of the ISM metallicity. As shown in [W. Wang et al. \(2025, in prep\)](#), the CGM around the ALPINE-CRISTAL-JWST galaxies is already significantly metal enriched, therefore some recycling of the already metal-enriched gas is expected. We find that the nominal  $\epsilon_{\text{out}}$  derived from the EAGLE (or FIRE-2) simulation underpredicts the metal abundance. Instead, a factor of two decreased outflow efficiency (or mass-loading factor) puts our model in better agreement with the observed MZR. Interestingly, such a weaker outflow efficiency (lower mass-loading factor) is also more consistent with the measured mass-loading factors ( $\epsilon_{\text{out}} \sim 1$  at  $\log(M/M_\odot) \sim 10$ ) of the ALPINE-CRISTAL galaxies ([M. Ginolfi et al. 2020](#); [J. E. Birkin et al. 2025](#)) as shown in Figure B.3 in Appendix B. These findings are consistent with [A. Pallottini et al. \(2025\)](#), which suggests a reduction of the outflow efficiency by a factor of two-thirds ( $\epsilon_{\text{SN}} \sim 0.3$ ). Observationally, the effect of outflows is difficult to constrain, as it depends on various physical quantities such as star formation, outflow velocity, or density of the ISM, which may all depend on redshift (e.g., [R. L. Davies et al. 2019](#)).

In summary, our simple analytical model describes well the overall MZR at  $z \sim 5$  of low-mass JWST-detected and massive ALPINE-CRISTAL-JWST galaxies. The range of observed metallicities at a given stellar mass (hence the MZR scatter) can, to first order, be explained by a mix of different stellar population ages, outflow efficiencies (mass-loading factors), and the metal enrichment of infalling gas. Notably, metals build up quickly to the observed levels within < 200 Myrs since the onset of star formation. To reproduce the most metal-poor systems, either very young (< 200 Myrs) stellar populations or efficient mass outflows (Figure 4) need to be assumed. Once concern here is that, due to the fast metal enrichment, any previous metal en-

**Table 3.** Scatter of the FMR measured at a given  $\mu$  (and  $\mu_0$ ) at different redshifts.

$z$	$\sigma_{\text{FMR}}$ (dex)	$\hat{\sigma}_{\text{FMR}}^\dagger$ (dex)	$\mu_0$	Reference
$z \sim 0$	0.02	< 0.02	0.22	(1)
	0.03	< 0.03	0.55	(2)
$z \sim 2.3$	0.16	0.06	0.60	(3)
$z \sim 3.3$	0.22	0.06	0.60	(3)
$z \sim 5$	0.24	0.13	0.66*	This work
	0.22	0.10	0.22	This work

NOTE— References: (1) [F. Mannucci et al. \(2010\)](#); (2) [M. Curti et al. \(2020\)](#); (3) [R. L. Sanders et al. \(2021\)](#).

$^\dagger$  FMR scatter deconvolved by measurement uncertainties.

\* Consistent with  $\mu_0 = 0.65$  obtained by [M. Curti et al. \(2024\)](#).

richment needs to be removed in order to observe them metal poor. This can be done by strong outflows or the accretion of pristine gas, or by spatially isolating the galaxies as it may be the case of a recently found metal-poor systems ([T. Morishita et al. 2025](#)). The most metal-rich systems are either old or have significantly less efficient outflows. Future, more detailed, observations of outflow rates from optical emission lines and the large-scale structure of the surrounding environment of these galaxies may help to distinguish these processes. In Section 4.2 we will further study the effect of a stochastic SFH, which may cause galaxies to scatter to lower metallicity.

Finally, we note that the observed metallicities are spatially integrated (consistent with the output of our analytical model). Spatially resolved metal abundances may show additional large variations. For example, pockets of recent star formation driven by pristine gas inflow may have lower-than-average metallicities ([J. Sánchez Almeida et al. 2014, 2015](#)). This is also further discussed in [S. Fujimoto et al. \(2025, in prep\)](#) and [F. Lopez et al. \(2025, in prep\)](#).

#### 4.2. Scatter of the FMR

As shown in the right panel of Figure 2, there is significant scatter in the FMR especially at lower stellar masses. For a  $\mu_0 = 0.66$  ([B. H. Andrews & P. Martini 2013](#)), we measure a scatter of  $\sigma_{\text{FMR}} \sim 0.24$  dex based on the data at  $z = 4 - 6$ . Similar to [F. Mannucci et al. \(2010\)](#), we have additionally tried to minimize the FMR scatter as a function of  $\mu_0$ . We found that  $\mu_0 = 0.22$  decreases the scatter to  $\sigma_{\text{FMR}} \sim 0.22$  dex, which is only slightly smaller than for  $\mu_0 = 0.66$ . The value of the scatter is consistent with [M. Curti et al. \(2024\)](#) at similar redshifts. We therefore use  $\mu_0 = 0.66$  here to be

consistent with other studies (B. H. Andrews & P. Martini 2013; M. Curti et al. 2020). The true FMR scatter is  $\hat{\sigma}_{\text{FMR}} = \sqrt{\sigma_{\text{FMR}}^2 - \sigma_{\text{meas}}^2} \sim 0.10 - 0.13 \text{ dex}$ , for  $\mu_0 = 0.22 - 0.66$  and assuming a conservative uncertainty in the metallicity measurement of  $\sigma_{\text{meas}} = 0.2 \text{ dex}$  (M. Curti et al. 2024). This is a factor of five larger than the scatter measured at  $z = 0$ ,  $\hat{\sigma}_{\text{FMR},0} \lesssim \sigma_{\text{FMR},0} = 0.02$  (F. Mannucci et al. 2010), and also significantly larger than at  $z \sim 2 - 3$ ,  $\hat{\sigma}_{\text{FMR}} \sim 0.06$  (R. L. Sanders et al. 2021). Note that the latter finds a  $\mu_0 = 0.60$  for the sample at  $z = 2.3$  and  $z = 3.3$ . Measurements of the FMR scatter at different redshifts are summarized in Table 3.

*Can this larger scatter be explained by a bursty star formation?* It is now well established that star formation is stochastic and bursty especially for galaxies at high redshifts and low stellar masses (e.g., G. Sun et al. 2025; A. L. Faisst & T. Morishita 2024; R. Endsley et al. 2024; R. Navarro-Carrera et al. 2024; L. Ciesla et al. 2024; J. B. Muñoz et al. 2023; X. Shen et al. 2023; Y. Asada et al. 2023; V. Mehta et al. 2023; A. L. Faisst et al. 2019; N. Emami et al. 2019; N. Caplar & S. Tacchella 2019; D. R. Weisz et al. 2012). This stochasticity may be driven by the outflow of gas through SNe feedback (specifically at low stellar masses), changes in gas accretion, and gas compaction and depletion events (e.g., C.-A. Faucher-Giguère 2018).

We further tested this scenario by directly using a stochastic SFH in our analytical model described in Section 4.1. Note that at this point, the model does not assume an equilibrium state anymore (contrary to the common “gas regulator” or “bathtub” model), but we directly compute the metal enrichment for an arbitrarily changing SFH. We adopt a stochastic (bursty) SFH as described in A. L. Faisst & T. Morishita (2024) and based on the mathematical prescription by N. Caplar & S. Tacchella (2019). Specifically, we use the `DELightcurveSimulation` Python package<sup>63</sup> (S. D. Connolly 2016), which is based on the D. Emmanoulopoulos et al. (2013) light-curve simulation algorithm. We assume a generalized power spectrum density (PSD, with a slope  $\alpha_{\text{PSD}} = 2$ ; A. L. Faisst & T. Morishita 2024). The stochastic SFH is parameterized by a burstiness amplitude ( $\sigma_{\text{MS}}$ ; *i.e.* the amplitude distance from the main-sequence in dex) and a correlation time ( $\tau_{\text{break}}$ ; *i.e.* roughly the  $\Delta t$  between amplitude peaks). We simulated SFHs with  $\sigma_{\text{MS}} = 0.1, 0.3$ , and  $0.6 \text{ dex}$  and  $\tau_{\text{break}} = 5, 50$ , and  $200 \text{ Myrs}$ . The latter is expected from simulations such as SPHINX<sup>20</sup> (J. Rosdahl et al.

2018, 2022; H. Katz et al. 2022; A. L. Faisst & T. Morishita 2024).

The resulting scatter of the FMR together with the observed scatter ( $\hat{\sigma}_{\text{FMR}}$ ) are shown in Figure 5, together with other analytical models discussed in Section 4.3. An increased burstiness amplitude increases the FMR scatter, but we do not find a significant dependency on  $\tau_{\text{break}}$  except for the largest  $\sigma_{\text{MS}}$ , where a shorter correlation time causes larger scatter. The scatter is largest at low stellar masses (corresponding to early times in a galaxy’s evolution and low  $\mu$ ) and decreases towards higher stellar masses. Furthermore, increased burstiness causes a *negative* (downward) scatter on the FMR similar to observational findings. These trends are caused when the metal abundance at later times saturates (as a matter of being a cumulative property similar to stellar mass), hence small scale variations in the metal production are less impactful at later times. We note that in our simple model the burstiness does not *per se* depend on stellar mass (more massive galaxies are expected to be less bursty, e.g. D. R. Weisz et al. 2012; N. Emami et al. 2019), hence the reduction of the scatter is purely due to the galaxy becoming more metal enriched over time. We find that a burstiness amplitude of  $\sigma_{\text{MS}} = 0.6 \text{ dex}$  can reproduce the observed scatter (deconvolved by measurement errors) well at high redshifts. However, a lower amplitude ( $\ll 0.3 \text{ dex}$ ) would be sufficient to explain the FMR scatter of low redshift galaxies. Our findings are consistent with a study by A. Pallottini et al. (2025), which shows, using a similar model, that the scatter of the MZR significantly depends on the burstiness of star formation.

We conclude that the scatter of the FMR at low metallicities (hence specifically low stellar masses) may be due to a bursty star formation history. Similar to observations, our bursty model suggests an asymmetric and negative FMR scatter. At later times, however, burstiness does not have a significant impact on the total observed metallicity. This may explain the smaller FMR scatter at low redshifts compared to higher redshifts. Furthermore, metal mixing may play a role. Figure 6 summarizes these conclusions.

#### 4.3. Comparison to Simulations and other Analytical Models

Our simple analytical model described in the previous sections reproduces well the observations at  $z \sim 5$  of the FMR and MZR. Furthermore, we showed that the *asymmetric* scatter in the FMR can be naturally explained by a stochastic star formation history. However, our simple model only provides limited predictions. For example, the burstiness of star formation is connected

<sup>63</sup> <https://github.com/samconnolly/DELightcurveSimulation>

to (or originates from) other physical processes such as gas outflows and star formation efficiencies or change in the gas inflows. In this section, we therefore compare the observations to predictions from cosmological simulations that include realistic feedback, outflow, inflow, and mass assembly.

The lower panel of Figure 1, shows the observations at  $z \sim 4 - 6$  (black crosses) compared to various cosmological simulations as well as other analytical models similar or more evolved than ours.

**SERRA Zoom-In Simulation** — The SERRA simulations are a set of zoom-in high-resolution ( $1.2 \times 10^4 M_{\odot}$ ,  $\simeq 25$  pc at  $z = 7.7$ ) cosmological simulations including non-equilibrium chemistry and on-the-fly radiative transfer (A. Pallottini et al. 2022). The masses of the galaxies range approximately between  $10^7 - 5 \times 10^9 M_{\odot}$ . Generally, the SERRA galaxies reproduce well the observed population in the mass range  $10^8 - 10^9 M_{\odot}$ , but they slightly overpredict and underpredict the metal abundances at lower and higher stellar masses, respectively (top panel, blue contours). The underprediction of metals in massive galaxies may be tied to the stochasticity of the SERRA galaxies as discussed in A. Pallottini et al. (2025).

**FIRE-2 Zoom-In Simulation** — FIRE-2 is a suite of cosmological zoom-in simulations including the implementation of realistic stellar and radiation feedback and winds (P. F. Hopkins et al. 2014, 2018; X. Ma et al. 2018a,b, 2019; P. F. Hopkins et al. 2023). The particle resolution is  $100 - 7000 M_{\odot}$  and the masses of the galaxies range from  $10^6 - 10^{10} M_{\odot}$  at  $z \sim 5$ . The MZR derived in A. Marszewski et al. (2024) (see also X. Ma et al. 2016) compares well to observations, although it slightly underpredicts the metal abundances at  $< 10^8 M_{\odot}$  (top panel, gray contours).

**THESAN-ZOOM Zoom-In Simulation** — This is a zoom-in to the cosmological simulation THESAN-1 (R. Kannan et al. 2022; A. Smith et al. 2022; E. Garaldi et al. 2022) at a baryonic mass and spatial resolution of  $142 M_{\odot}$  and  $\sim 17$  cpc, respectively. It includes self-consistently the effects of supernova feedback, radiation fields, dust physics, and low temperature cooling via molecular hydrogen (F. Marinacci et al. 2019; R. Kannan et al. 2020, 2021). We use the MZR prediction presented in R. Kannan et al. (2025) and find a good agreement with the observed relation (bottom panel, pink dot-hatched). However, we notice that the spread in metallicity is significantly narrower than that observed.

**NEWHORIZON Zoom-in Simulation** — The NEWHORIZON project (Y. Dubois et al. 2021) performs a high-

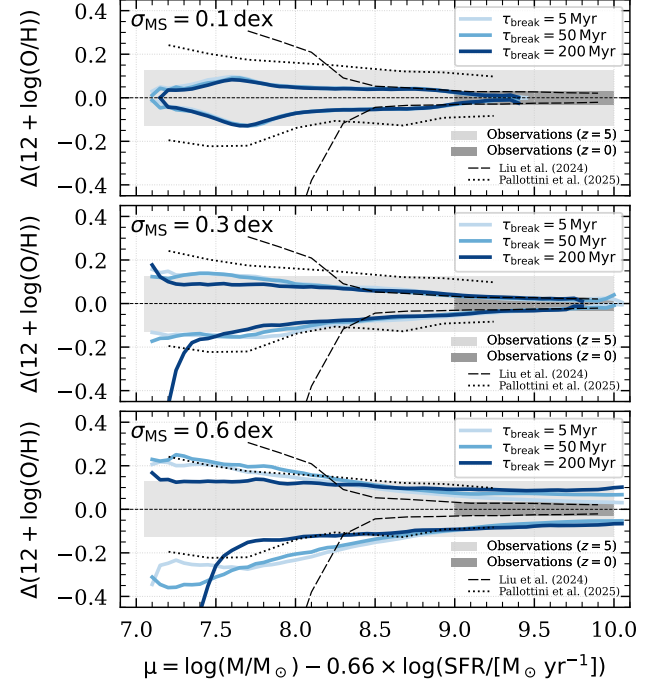


**Figure 5.** Scatter of the FMR as a function of  $\mu$  for different assumption of burstiness of the SFH. The SFH is described by a burstiness amplitude ( $\sigma_{\text{MS}}$ , different panels) and a correlation timescale ( $\tau_{\text{break}}$ , shades of blue). The observed FMR scatter (deconvolved by measurement errors) at  $z \sim 5$  and  $z = 0$  is shown in light and dark gray, respectively. We also show the scatter derived from the analytical models from L.-J. Liu et al. (2024) (long-dashed line) and A. Pallottini et al. (2025) (dotted line).

resolution zoom-in simulation extracted from the parent simulation HORIZON-AGN ((142 Mpc) $^3$ ; Y. Dubois et al. 2014) in a box size of  $(16 \text{ Mpc})^3$  and a resolution of up to 34 pc. These simulations are generally in good agreement with the observed MZR at stellar masses of  $< 10^9 M_{\odot}$  (top panel, green contours). However, the scatter is narrow and the sample size at higher stellar masses is small, both likely due to the small volume probed by the simulation.

**SPHINX<sup>20</sup> Simulation** — The SPHINX<sup>20</sup> is a full box cosmological radiation hydrodynamics simulation optimized to simulate cosmic reionization and the multiphase ISM of high- $z$  galaxies to provide statistical samples of galaxies similar to those currently being observed by JWST (J. Rosdahl et al. 2018, 2022; H. Katz et al. 2023). The metallicity measurement are taken from the current data release described in H. Katz et al. (2023). These simulations generally underpredict the metal abundances of  $z \sim 5$  galaxies (bottom panel, blue dot-hatched) and occupy a similar parameter space as

the FIRE-2 galaxies in terms of stellar mass and metallicity.

*ILLUSTRISTNG Simulation* — ILLUSTRISTNG is a suite of large volume, cosmological, gravomagnetohydrodynamical simulations, covering  $302.6^3$ ,  $106.5^3$ , and  $51.7^3$  cMpc $^3$ , respectively, and particle resolutions between  $10^4 - 10^7 M_{\odot}$  (F. Marinacci et al. 2018; J. P. Naiman et al. 2018; D. Nelson et al. 2018, 2019; V. Springel et al. 2018; A. Pillepich et al. 2018, 2019). We compare the observations to the resulting MZR for stellar masses of  $10^8 - 10^{11} M_{\odot}$  from M. Hirschmann et al. (2023), who derived accurate optical emission line for the simulated galaxies in post-processing (bottom panel, yellow band). The predicted metal abundances reproduce well the observations.

*DUSTY-GAEA Simulation* — DUSTY-GAEA is a modified version of the state-of-the-art semi-analytic GALaxy Evolution and Assembly (GAEA; G. De Lucia et al. 2014; M. Hirschmann et al. 2016; L. Xie et al. 2020; F. Fontanot et al. 2020; G. De Lucia et al. 2024) model, where a dust physical prescription is included in a self-consistent manner (O. Osman et al. 2025, in prep.). The DUSTY-GAEA model is run on the MILLENIUM (V. Springel et al. 2005) and MILLENIUM II (M. Boylan-Kolchin et al. 2009) merger trees to cover the wide range of the stellar mass ( $\log(M/M_{\odot}) > 7$ ) on the MZR plane. This model describes well the observed MZR (bottom panel, purple forward-hatched).

*L. Pantoni et al. (2019) Analytical Model* — Similar to our model, this analytical model self-consistently describes the spatially averaged time evolution of the gas, stellar, metal, and dust contents (see also A. Lapi et al. 2020), based on the model by A. Lapi et al. (2017). It is thought to better represent high- $z$  galaxies and progenitors of early type galaxies compared to constant gas inflow models. It reproduces well the overall metal abundances, however, it slightly overestimates the metallicity of the most massive galaxies (bottom panel, green backward-hatched).

*A. Pallottini et al. (2025) Analytical Model* — This minimal physical model, directly tied to the dark matter halo growth, is similar in general to the one used in this work. The model has adjustable SNe delay, feedback, and variable accretion rate to simulate an oscillating, bursty SFH. Here we use the model “weak feedback and modulated accretion”, which reproduces the observed MZR well (bottom panel, orange downward-hatched). As shown in Figure 5, this model leads to a similar scatter in the FMR as our stochastic SFH model assuming  $\sigma_{\text{MS}}$  scatter between  $0.3 - 0.6$  dex and recovers well the

observed FMR scatter at  $z \sim 5$  (however, it slightly over-predicts the FMR scatter at the lowest stellar masses). Note that the scatter reported here from A. Pallottini et al. (2025) is the maximal range of models (not the  $1\sigma$  value). Importantly, a decreasing trend of FMR scatter with stellar mass is reported as well by this model.

*L.-J. Liu et al. (2024) Analytical Model* — This physically motivated analytical model takes a similar approach as A. Pallottini et al. (2025). It implements a modulated SFH as a result of delayed injection of supernova feedback (S. R. Furlanetto & J. Mirocha 2022) in a self-regulated disk model as the basis for describing galaxy-scale star formation (see also C.-A. Faucher-Giguère et al. 2013; C.-A. Faucher-Giguère 2018). It self-consistently models the gas, stellar, metal contents, and line emissions that trace the star formation. Adopting the scenario with galactic wind driven by reduced supernova feedback (smaller mass-loading factor), this model matches the measured MZR (gray, lower panel Figure 1) and is broadly consistent with the observed  $1\sigma$  scatter of the FMR derived from our stochastic SFH model (Figure 5). However, the scatter of metallicity predicted by this model is larger than observed at stellar mass of  $< 10^8 M_{\odot}$ . This can be induced by the burstiness in low-mass galaxies whose shallow gravitational potentials are unlikely to prevent metal contents from being evacuated by feedback-driven outflows.

We note that most simulations reproduce the scatter of the observed metal abundances at a given stellar mass. This shows that the scatter in the MZR is dominated by physical processes and not measurement uncertainties (see also Section 4.1). The reason that some cosmological simulations underpredict the metal abundances could be due to limited volume coverage to simulate galaxies that have above-average metal enrichment (e.g., fast evolving galaxies). For example, the FIRE-2 simulation covers  $\sim (43 \text{ cMpc})^3$  and the SPHINX<sup>20</sup> simulation covers  $\sim (20 \text{ cMpc})^3$ , which are both significantly smaller volumes than covered by observations ( $\sim (100 \text{ cMpc})^3$ ). This may be connected to failing to reproduce the significant ALMA far-infrared [O III] $_{88 \mu\text{m}}$  emission in two  $z > 12$  galaxies (see discussion in S. Yang et al. 2025). However, other differences such as the implementation of feedback, radiative heating and cooling, or chemical models may also change the resulting metal enrichment. Lastly, observational constraints may still hinder the detection of low-metallicity galaxies at high redshifts. This could be mitigated by observing lensed high-redshift galaxies (e.g., B. Welch et al. 2025; L. Christensen et al. 2012a,b; E. Vanzella et al. 2023).

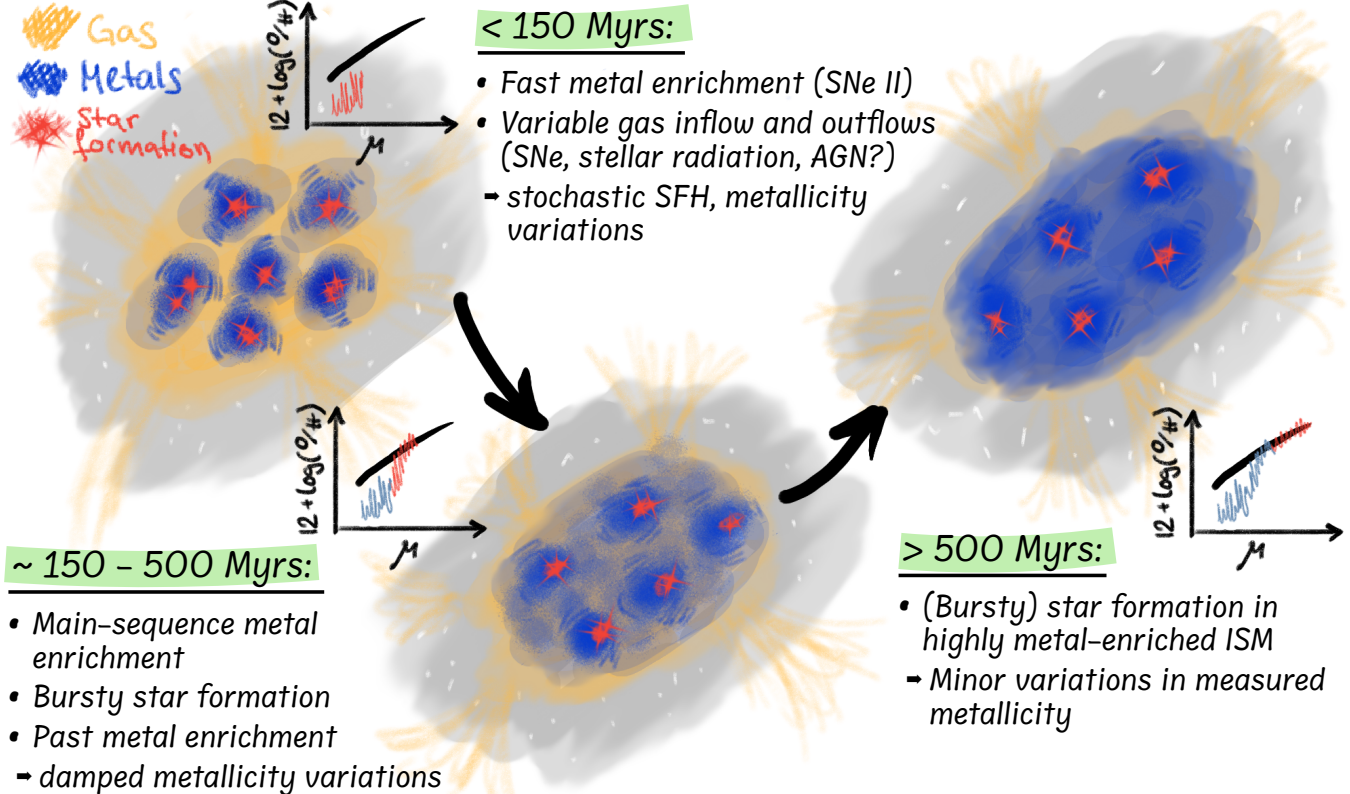


**Figure 6.** Sketch of the early metal enrichment of galaxies. Gas (yellow), metals (blue), and areas of active star formation (red) are indicated. Metal enrichment is indicated as blue arcs and gas inflow as yellow streams. The inset figures show the current location and scatter (red) of the galaxy at a given time on the FMR. Young galaxies experience fast metal enrichment with large scatter on MZR and FMR due to stochastic star formation caused by variable gas inflows and outflows. Older galaxies continue to have bursty star formation but with damped MZR/FMR scatter due to past metal enrichment.

#### 4.4. The progenitors and descendants of the ALPINE galaxies

We use the DUSTY-GAEA simulation model (O. Osman et al. 2025, in prep) to characterize the evolutionary path of the ALPINE-CRISTAL-JWST galaxies on the MZR and FMR plane. We chose DUSTY-GAEA because it is able to reproduce well the metal abundances over the full stellar mass range of galaxies at  $z \sim 5$  (Figure 1) as well as lower redshifts (F. Fontanot et al. 2024).

We chose  $\sim 2400$  representative galaxies in the DUSTY-GAEA model that cover the range of metallicity ( $12 + \log(\text{O/H}) = 7.8 - 8.7$ ), SFR ( $\log(\text{SFR}/[\text{M}_\odot \text{ yr}^{-1}]) = 1.2 - 2.3$ ), and stellar mass ( $10^{9.5} - 10^{10.9} \text{ M}_\odot$ ) of the ALPINE-CRISTAL-JWST sample. We then trace the galaxies backward and forward in time by following their merger trees. We use both Millennium (V. Springel et al. 2005) and Millennium II (M. Boylan-Kolchin et al. 2009) merger trees to cover the wide range of the stellar mass ( $\log(M/\text{M}_\odot) > 7$ ).

The left panel of Figure 7 shows the MZR including observations at  $z = 4 - 6$  (ALPINE-CRISTAL-

JWST galaxies indicated with large black symbols). The simulated DUSTY-GAEA tracks of the ALPINE-CRISTAL-JWST progenitor galaxies are indicated as red lines from redshifts  $z = 15$  to  $z = 5$  (indicated by red dots). The blue line shows the tracks of the descendants from  $z = 5$  to  $z = 0$  (indicated by blue dots). The red/blue cloud shows the range of galaxy model progenitors/descendants marginalized over all those simulated galaxies. The tracks themselves connect the median values at a given redshift snapshot. The progenitors of the ALPINE-CRISTAL-JWST galaxies follow a slightly sloped MZR to  $z \sim 10$  ( $\sim 700$  Myrs in the past) after which there are indications that the relation drops off more steeply to lower metallicities (note that the time difference from  $z = 10$  to  $z = 15$  is only  $\sim 250$  Myrs).

One caveat is that the MILLENIUM simulation only sparsely populates the regime at  $z > 9$ . We therefore compared the progenitor tracks to  $\sim 400$  galaxies from the Planck Millennium simulation (PMILL; C. M. Baugh et al. 2019). This  $N$ -body simulation is updated with the recent Planck cosmology (Planck Collaboration et al. 2014) and supports a higher resolution and better time sampling at high redshifts than the MILLEN-

NUM simulation. Making use of this increased sampling we found a slightly less steep metallicity evolution beyond  $z = 9$ , but overall consistent with the previous results.

The comparison to simulations emphasizes the fast build-up of metals at early times before flattening off to join a more mature main-sequence evolution of metals over time, characterized by the local FMR. Note that this is consistent with our simple analytical model (Figure 4), showing younger galaxies at lower metallicity at a given stellar mass. Furthermore, such a transition has been discussed in D. Burgarella et al. (2025), suggesting a possible shift in the mechanism of metal and dust production around a critical metallicity of  $12 + \log(\text{O/H}) \sim 7.6$  from being dominated by stellar-dust production (mainly from SNe) to grain growth through gas-dust accretion in the ISM.

This early build-up of metals is further visualized on the FMR (right panel, Figure 7). The progenitors of the ALPINE-CRISTAL-JWST galaxies start to “fall off” the local relation around  $z \sim 10$  as they have a significantly ( $> 3\sigma$ , indicated by the gray bands) lower metallicity at a given  $\mu$  compared to the  $z = 4 - 6$  observed population and the local relation. This suggests that the ALPINE-CRISTAL-JWST progenitors join the fundamental metallicity relation to proceed, after a rapid build-up of metals, with more mature metal build-up. Again, we note that for the MILLENNIUM simulation, only 22 snapshots were saved at redshift  $> 5$ . Therefore our statements about the rapid growth of metals at early times should be interpreted with caution. Nevertheless, from preliminary work based on simulations with a much larger number of snapshots (such as PMILL), results are qualitatively similar to those shown and discussed here. We will address this more explicitly in a forthcoming work (O. Osman et al. 2025, in prep).

Based on the DUSTY-GAEA models, the  $z \rightarrow 0$  descendants of the ALPINE-CRISTAL-JWST sample galaxies are massive ( $\log(M_*/M_\odot) \sim 11.4$ ) with (super-solar) metallicities of  $12 + \log(\text{O/H}) \sim 9$ . The descendants follow well the expected FMR until  $z \sim 2$ . After that, they become quiescent and their SFR drops from  $\sim 60 M_\odot \text{ yr}^{-1}$  ( $z = 2$ ) to  $\sim 2 M_\odot \text{ yr}^{-1}$  at  $z = 0$ . At that point they leave the FMR of star-forming galaxies as shown on the right panel of Figure 7.

As comparison, we also show the approximate location of our own Milky Way in Figure 7. The total stellar mass ( $6.08 \pm 1.14 \times 10^{10} M_\odot$ ) is taken from T. C. Licquia & J. A. Newman (2015) and the SFR ( $2.0 \pm 0.7 M_\odot \text{ yr}^{-1}$ ) from D. Elia et al. (2022). The Milky Way’s gas-metallicity is less constrained due to different calibrations and radial dependence. Here we assumed

$12 + \log(\text{O/H}) \sim 8.75$  (S. Daflon & K. Cunha 2004; L. S. Pilyugin et al. 2006; M. Mollá et al. 2019). The descendants of the ALPINE-CRISTAL-JWST galaxies are predicted to be five times more massive and have  $\sim 0.2$  dex higher oxygen abundances. However, we note most of the metals at  $z < 1$  are bound in stars, which would mean that the actual ISM metallicities of the simulated ALPINE  $z = 0$  galaxies are lower (C. Péroux & J. C. Howk 2020).

In conclusion, the simulations show a consistent picture in which the ALPINE-CRISTAL-JWST galaxies build up their metals quickly in the first  $\sim 200$  Myrs before joining the local fundamental relation around  $z = 10$ . We now observe the mature evolution of the metal abundances, moving towards solar metallicity at the highest masses at  $z = 5$ . This evolution continues down to  $z = 0$ . In other words, to witness the early build up of metals, galaxies at  $z > 10$  need to be observed, or alternatively much younger galaxies at later times.

## 5. SUMMARY & CONCLUSIONS

We have used the ALPINE-CRISTAL-JWST survey data to investigate the spatially integrated metal enrichment of 18 massive ( $\log(M_*/M_\odot) = 9.5 - 11$ ) galaxies at  $z \sim 5$ . This sample is complementary to previous studies of JWST-observed samples that probe lower stellar masses, hence allows insights into the metal enrichment of the massive early galaxies. The metallicities are derived using the strong-line method (A. Faisst et al. 2025, submitted) applying the R. L. Sanders et al. (2024) calibration. We find good agreement with  $T_e$ -based metallicity estimates for five galaxies for which such measurements are possible. The  $T_e$  values vary at  $\sim 1 - 2 \times 10^4 \text{ K}$  and electron densities are between  $n_e = 200 - 1000 \text{ cm}^{-3}$  with an average of  $400 \text{ cm}^{-3}$ . The main observational findings of our study are the following:

- Corroborating on the full stellar mass range of samples from the literature and from the ALPINE-CRISTAL-JWST sample, we found a relatively shallow mass-metallicity relation at  $z \sim 5$  (Equation 1; Figure 1). This suggests a significant (and fast) metal enrichment even at low stellar masses. Overall, massive  $z = 5$  galaxies show similar metal abundances as galaxies at cosmic noon at similar masses.
- Galaxies at  $z \sim 5$  are to first order consistent with the local FMR. To second order, the  $z \sim 5$  FMR shows a downward scatter in metallicity at a fixed stellar mass (or  $\mu$ ) compared to the local relation

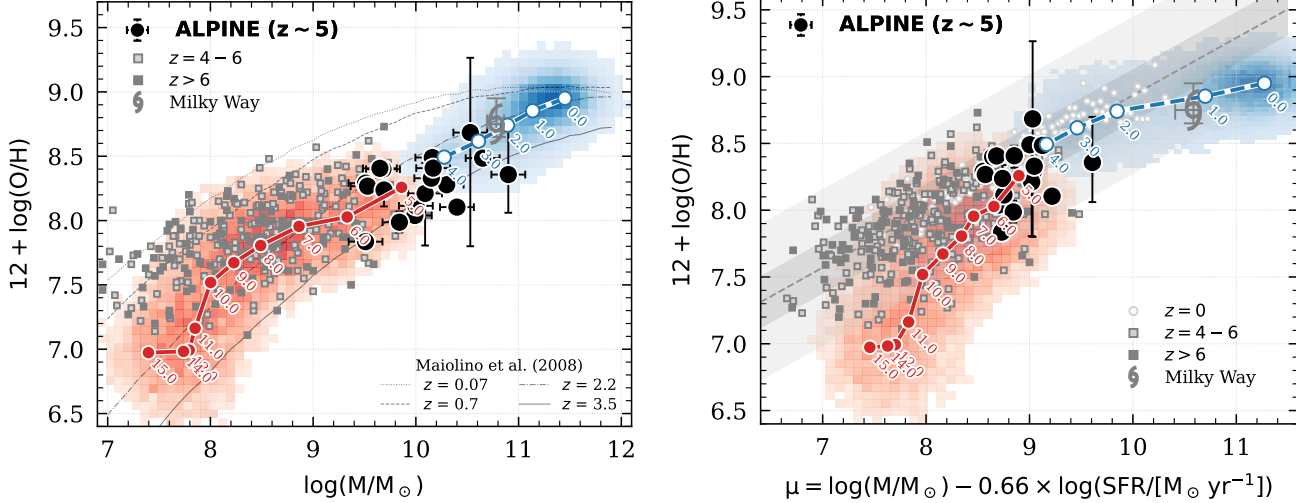


**Figure 7.** Tracks of simulated DUSTY-GAEA model progenitors (red) and descendants (blue) of the ALPINE-CRISTAL-JWST sample. *Left:* The MZR with observations at  $z = 4 - 6$  (gray squares) and  $z > 6$  (solid dark gray squares) as well as our Milky Way (§) indicated. The ALPINE-CRISTAL-JWST sample is indicated with large black circles. The MZR parameterizations from R. Maiolino et al. (2008) at different redshifts are indicated as thin lines. The DUSTY-GAEA models (matched to the ALPINE-CRISTAL-JWST galaxies in metallicity, SFR, and stellar mass) are shown in red ranging from  $z = 5$  to  $z = 15$  ( $\Delta t = 1$  Gyr, redshifts indicated by red dots) and blue from  $z = 5$  to  $z = 0$ . The red/blue cloud shows the possible range of progenitor/ancestor tracks. *Right:* Same as left panel, but showing the FMR. The local FMR (B. H. Andrews & P. Martini 2013) is shown as dashed line. The  $1\sigma$  and  $3\sigma$  scatter of the  $z = 4 - 6$  observations around this local relation are shown as light and dark gray bands, respectively.

(Figure 2). This could indicate the early phases of metal enrichment.

- We find the intrinsic scatter of the FMR at  $z \sim 5$  to be approximately five times larger compared to the local FMR (Figure 5 and Table 3).

We investigated these findings further in the light of a simple analytical model. Our model is similar to previous “gas-regulator” prescriptions (e.g. S. J. Lilly et al. 2013; R. Feldmann 2015), however, instead of using a constant yield, we have implemented a metal enrichment based on more realistic metal yields of type II SNe and AGB stars (Figure 3). Furthermore, we use stellar mass and redshift-dependent mass-loading factors derived from the EAGLE simulation. Comparing the observations across the full mass range to this analytical model as well as to the latest cosmological simulations we further conclude:

- Our analytical model reproduces well the observed MZR assuming reasonable values for the gas depletion times, gas accretion rates, and the metallicity of infalling gas. However, we find that a  $\sim 2\times$  lower outflow efficiency (*i.e.* lower mass-loading factor) than found by the EAGLE and FIRE simulations is preferred to reproduce the MZR at  $z = 5$  (Figure 4).

- Our model suggests a fast metal enrichment. The observed metallicities at  $z = 5$  can be reached in less than 200 Myrs. Furthermore, the range of metallicities *at a given stellar mass* is set by the stellar population age, the metallicity of inflowing gas, and outflow efficiency (mass-loading factor) (Figure 4). Due to the fast metal enrichment, metal-poor systems need either very efficient outflows ( $> 2\times$  more efficient than simulations predict) or pristine gas inflows.

- The observed downward scatter of the FMR at a given stellar mass or ( $\mu$ ) can be explained naturally by a bursty star formation (Figure 5). Less scatter is expected for more metal-rich galaxies, which can explain the  $5\times$  lower scatter in the local FMR.
- Cosmological simulations generally reproduce the observed MZR, however, they tend to underpredict the metal enrichment of low-mass ( $\log(M/M_\odot) < 8.5$ ) galaxies (Figure 1). This may be because of the lack of simulated volume or dark matter halo resolution, or too slow enrichment of metals over time or too efficient outflows.
- The DUSTY-GAEA simulation (which fits the observed MZR well at all stellar masses) suggests that the ALPINE-CRISTAL-JWST galaxies build up their metal abundance quickly at  $z = 15 - 10$ ,

and then joined the observed  $z = 5$  FMR (Figure 7). The galaxies will then enrich further with metals to reach super-solar values at stellar masses of  $\log(M/M_\odot) > 11.4$  ( $5\times$  more massive than our Milky Way). They will leave the FMR relation at  $z = 2$  when star formation starts to get quenched.

Overall, galaxies at  $z \sim 5$  are already significantly metal enriched at all stellar masses. The difference in metal-enrichment at a given stellar mass can be explained by the evolutionary age of the galaxies but also by differences in outflow efficiency and the metallicity of the accreted gas. The scatter in both the MZR and FMR can be reproduced by a stochastic SFH, but only at low masses at the onset of metal enrichment. Figure 6 summarizes these conclusions.

The outflow efficiency plays an important role in reproducing the observed MZR at  $z \sim 5$  as well as the observed [C II] halos surrounding galaxies at the same epoch (e.g., S. Fujimoto et al. 2019). As discussed in our work and in A. Pallottini et al. (2025), the outflows in simulations may be too efficient in removing metal-rich gas, causing an underestimation of the MZR. At the same time, lowering the outflow efficiency to fit the MZR may result in simulations not reproducing the extended [C II] halos (e.g., L.-J. Liu et al. 2025, in prep; W. Wang et al. 2025, in prep). Now, with more statistical data available, resolving this discrepancy may become an interesting topic in the near future.

## ACKNOWLEDGMENTS

This work is based in part on observations made with the NASA/ESA/CSA *James Webb* Space Telescope. The JWST and HST data presented in this article were obtained from the Mikulski Archive for Space Telescopes (MAST) at the Space Telescope Science Institute. These observations are associated with programs, HST-GO-13641 (doi: [10.17909/xne1-7v26](https://doi.org/10.17909/xne1-7v26)), JWST-GO-01727 (doi: [10.17909/ph8h-qf05](https://doi.org/10.17909/ph8h-qf05)), JWST-GO-03045 (doi: [10.17909/cqds-qc81](https://doi.org/10.17909/cqds-qc81)), and JWST-GO-04265 (doi: [10.17909/wac6-9741](https://doi.org/10.17909/wac6-9741)). This research has made use of the NASA/IPAC Infrared Science Archive (IRSA), which is funded by the National Aeronautics and Space Administration and operated by the California Institute of Technology. The following dataset was used from IRSA: doi: [10.26131/IRSA178](https://doi.org/10.26131/IRSA178). Support for program JWST-GO-03045 was provided by NASA through a grant from the Space Telescope Science Institute, which is operated by the Association of Universities for Research in Astronomy, Inc., under NASA contract NAS 5-03127. This paper makes use of the following ALMA data: ADS/JAO.ALMA#2017.1.00428.L,

#2019.1.00226.S, #2022.1.01118.S, and #2021.1.00280.L. ALMA is a partnership of ESO (representing its member states), NSF (USA) and NINS (Japan), together with NRC (Canada), MOST and ASIAA (Taiwan), and KASI (Republic of Korea), in cooperation with the Republic of Chile. The Joint ALMA Observatory is operated by ESO, AUI/NRAO and NAOJ. This work made use of Astropy:<sup>64</sup> a community-developed core Python package and an ecosystem of tools and resources for astronomy (Astropy Collaboration et al. 2013, 2018, 2022). ALF thanks Jennifer Tan for proofreading the manuscript. AF is partly supported by the ERC Advanced Grant INTERSTELLAR H2020/740120, and by grant NSF PHY-2309135 to the Kavli Institute for Theoretical Physics. AN acknowledge support from the Narodowe Centrum Nauki (NCN), Poland, through the SONATA BIS grant UMO-2020/38/E/ST9/00077. CG acknowledges support from the ASI-INAF agreement n. 2025-6-HH.0. DBS gratefully acknowledges support from NSF Grant 2407752. DGE acknowledges support from ANID BECAS/DOCTORADO NACIONAL/2024-21251071. EdC acknowledges support from the Australian Research Council through project DP240100589. EI gratefully acknowledge financial support from ANID - MILENIO - NCN2024\_112 and ANID FONDECYT Regular 1221846. HÜ acknowledges funding by the European Union (ERC APEX, 101164796). Views and opinions expressed are however those of the authors only and do not necessarily reflect those of the European Union or the European Research Council Executive Agency. Neither the European Union nor the granting authority can be held responsible for them. IDL acknowledges funding from the European Research Council (ERC) under the European Union’s Horizon 2020 research and innovation program DustOrigin (ERC-2019-StG-851622), from the Belgian Science Policy Office (BELSPO) through the PRODEX project “JWST/MIRI Science exploitation” (C4000142239) and from the Flemish Fund for Scientific Research (FWO-Vlaanderen) through the research project G0A1523N. JM gratefully acknowledges support from ANID MILENIO NCN2024\_112. JS is supported by JSPS KAKENHI (JP22H01262). KVGC was supported by NASA through the STScI grants JWST-GO-04265 and JWST-GO-03777. LV acknowledges support from the INAF Minigrant “RISE: Resolving the ISM and Star formation in the Epoch of Reionization” (PI: Vallini, Ob. Fu. 1.05.24.07.01). NGV acknowledges scholarship from ANID BECAS/Doctorado Nacional/2023-21231942. MA is supported by FONDECYT grant number 1252054, and gratefully acknowledges support from ANID Basal Project FB210003 and ANID MILENIO NCN2024\_112. MB gratefully acknowledges support from

<sup>64</sup> <http://www.astropy.org>

the ANID BASAL project FB210003. This work was supported by the French government through the France 2030 investment plan managed by the National Research Agency (ANR), as part of the Initiative of Excellence of Université Côte d’Azur under reference number ANR-15-IDEX-01. MR acknowledges support from project PID2023-150178NB-I00 financed by MCIU/AEI/10.13039/501100011033, and by FEDER, UE. RA acknowledges financial support from projects PID2023-147386NB-I00 funded by MCIN/AEI/10.13039/501100011033 and by ERDF/EU and the Severo Ochoa grant CEX2021-001131-S to the IAA-CSIC. RJA was supported by FONDECYT grant number 1231718 and by the ANID BASAL project FB210003. SF acknowledges support from NASA through the NASA Hubble Fellowship grant HST-HF2-51505.001-A awarded by the Space Telescope Science Institute, which is operated by the Association of Universities for Research in Astronomy, Incorporated, under NASA contract NAS5-26555. VV acknowledges support from the ANID BASAL project FB210003 and from ANID MILENIO NCN2024\_112.

*Facilities:* HST(ACS), HST(WFC3/IR), JWST(NIRCam), JWST(NIRSpec), ALMA

*Software:* `Astropy` ([Astropy Collaboration et al. 2013, 2018](#)), `PyNeb` ([V. Luridiana et al. 2015](#))

## APPENDIX

## A. DETAILS ON METALLICITY CALCULATIONS

The left panel of Figure A.1 compares oxygen abundances based on the calibration from R. L. Sanders et al. (2024) with the one of R. Maiolino et al. (2008) (see also T. Nagao et al. 2006). We do not find significant differences between these calibrations within the uncertainties of the measurements. The same holds for the calibration by M. Hirschmann et al. (2023), which is similar to the one from R. L. Sanders et al. (2024) that is used here.

In some cases, we are able to compare the strong line metallicity measurements to the oxygen abundances independently derived from fainter optical auroral lines (the “ $T_e$  method”, see review on metallicity measurements in L. J. Kewley et al. 2019). These lines are only detected in a handful of galaxies; however, their detections allows an independent comparison to the metal abundances based on the strong line method. We derived the oxygen abundances using the `getTemDen` module of the PyNeb Python package (V. Luridiana et al. 2015) from the electron temperatures ( $T_e(O^+)$  and  $T_e(O^{++})$ ) and the electron density ( $n_e$ ) by following these steps.

1. We derived  $T_e(O^{++})$  from the  $[\text{O III}]_{4363}/[\text{O III}]_{5007}$  line ratio. For this we assumed  $n_e = 400 \text{ cm}^{-3}$ , however, the exact value is not important as this measurement is independent of  $n_e$  (middle panel, Figure A.2).
2. We derived  $n_e$  using the  $[\text{S II}]_{6732}/[\text{S II}]_{6718}$  line ratio, assuming an electron temperature of  $2 \times 10^4 \text{ K}$  (again, this assumption is not critical as the dependence on electron temperature is weak, see right panel of Figure A.2).
3. We used the derived electron density to compute  $T_e(O^+)$  using the line ratio  $([\text{O II}]_{7322} + [\text{O II}]_{7332})/[\text{O II}]_{3727}$  (left panel, Figure A.2).
4. Finally, using the `getIonAbundance` module of PyNeb, we computed the oxygen abundances  $\frac{\text{O}^+}{\text{H}}$  and  $\frac{\text{O}^{++}}{\text{H}}$  from the  $[\text{O II}]_{3727}/\text{H}\beta$  and  $([\text{O III}]_{5007} + [\text{O III}]_{4959})/\text{H}\beta$  line ratios and the above measured electron temperatures ( $T_e(O^+)$  and  $T_e(O^{++})$ ) and electron density  $n_e$ .

Note that we neglect higher ionization species in this calculation as they are not expected to significantly contribute to the total abundance.

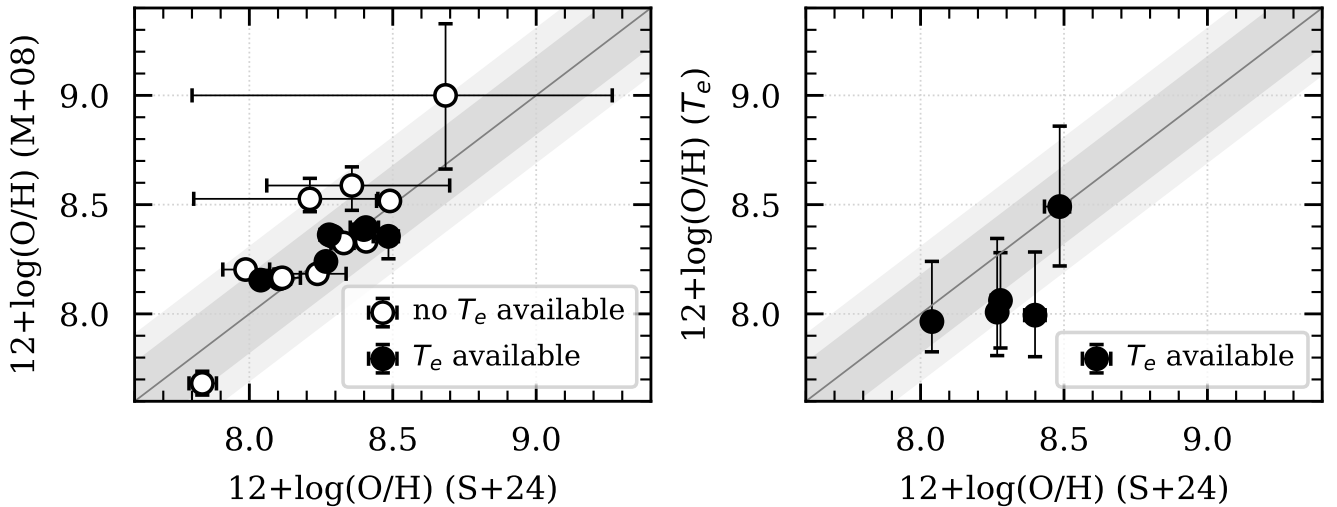


**Figure A.1.** *Left:* Comparison of metallicity calculations based on the strong-line parameterizations from R. Maiolino et al. (2008) (and T. Nagao et al. 2006) and R. L. Sanders et al. (2024). Filled symbols indicate the five galaxies with robust electron temperature measurements. *Right:* Comparison of metallicity calculations based on the strong-line method (using calibration by R. L. Sanders et al. 2024) and the direct  $T_e$  method measured from these data. This measurement is only available for five galaxies (filled symbols). In both panels, the light and dark gray bands show deviations of 50% and a factor of two ( $\sim 0.3 \text{ dex}$ ), respectively.

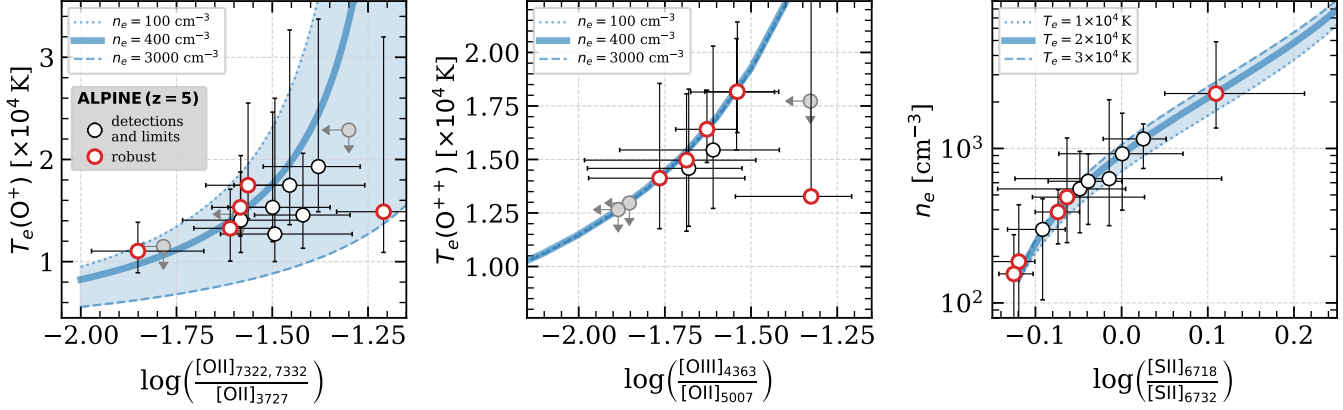


**Figure A.2.** Relation between line ratios, electron temperatures, and electron density derived from PyNeb (blue) including the measurements of the ALPINE-CRISTAL-JWST targets (symbols). The five galaxies indicated in red have the most robust  $T_e$ -based metallicity measurements (see also Figure A.1).

In summary, we find electron temperatures of  $1 - 2 \times 10^4$  K and electron densities of  $100 - 1000 \text{ cm}^{-3}$  ( $\langle n_e \rangle \sim 400 \text{ cm}^{-3}$ ). These values are consistent with other measurements performed by JWST on galaxies of similar mass, SFR, and redshift (e.g. from the *AURORA* survey; M. W. Topping et al. 2025). The uncertainty in these parameters and the derived metal abundances are substantial due to the low signal-to-noise ratio of the auroral lines. We therefore only considered galaxies to have robust  $T_e$ -based metallicity measurements if they have a robust (< 50% uncertainty) detection of the [O III]4363, [O II]7322, and [O II]7332 lines. The five galaxies that pass this criteria are indicated in red in Figure A.2; DC-417567, DC-630594, DC-709575, DC-842313, and DC-873321. The right panel of Figure A.1 shows a comparison of the  $T_e$  and strong-line based metallicity measurements for these five galaxies. We find a good agreement between these independent measurements within the uncertainties, suggesting that our strong-line metal abundance estimates are reasonable.

## B. DETAILS ON MASS-LOADING FACTOR

The outflow properties, specifically the mass-loading factor ( $\epsilon_{\text{out}}$ ), is closely linked to the evolution of galaxies. In our model, the outflow of metal-rich gas significantly affects the overall predicted metallicity. Importantly, the mass-dependence of  $\epsilon_{\text{out}}$  relates to the steepness of the MZR.

Here, we use the characterization of  $\epsilon_{\text{out}}(M, z)$  as found in the EAGLE simulation (J. Schaye et al. 2015; R. A. Crain et al. 2015), specifically as presented in figure 3 of P. D. Mitchell et al. (2020). To be able to use this result in our model, we derived an analytical representation in the form of a double power-law as follows:

$$\frac{\langle \dot{M}_{\text{wind,ISM}} \rangle}{\langle \dot{M}_* \rangle} \equiv \epsilon_{\text{out}} = \xi^{-1}(M_*, z), \quad (\text{B1})$$

with

$$\xi(M_*, z) = \frac{\phi^*(z)}{10^{(\delta+1) \times (\log(M_{\text{star}}) - \mathcal{M})} + 10^{(\gamma+1) \times (\log(M_{\text{star}}) - \mathcal{M})}}, \quad (\text{B2})$$

where we define  $\phi^*(z) = 10^{1.1 - (1+z)^{0.09}}$ ,  $\mathcal{M}(z) = 8.2 + (1+z)^{0.29}$ ,  $\delta(z) = -0.4 - (1+z)^{0.02}$ , and  $\gamma(z) = 0.05 - (1+z)^{0.01}$ .

We find that this parameterization gives consistent results to A. L. Muratov et al. (2015), which is based on the FIRE simulation (P. F. Hopkins et al. 2014).

Figure B.3 compares this theoretical mass-loading factor to observations. The red hatched region shows the approximate area of the observed mass-loading factors of the ALPINE galaxies (M. Ginolfi et al. 2020; J. E. Birkin et al. 2025). The blue circles show the location of local starburst from T. M. Heckman et al. (2015) and the turquoise star denotes the measurement for HZ4 at  $z \sim 5$  from R. Herrera-Camus et al. (2021). Most of the local starbursts as well as HZ4 are consistent with the nominal mass-loading factor derived from the EAGLE simulation. However, the ALPINE galaxies are more consistent with an outflow efficiency reduced by a factor of two. Interestingly, such a reduction of

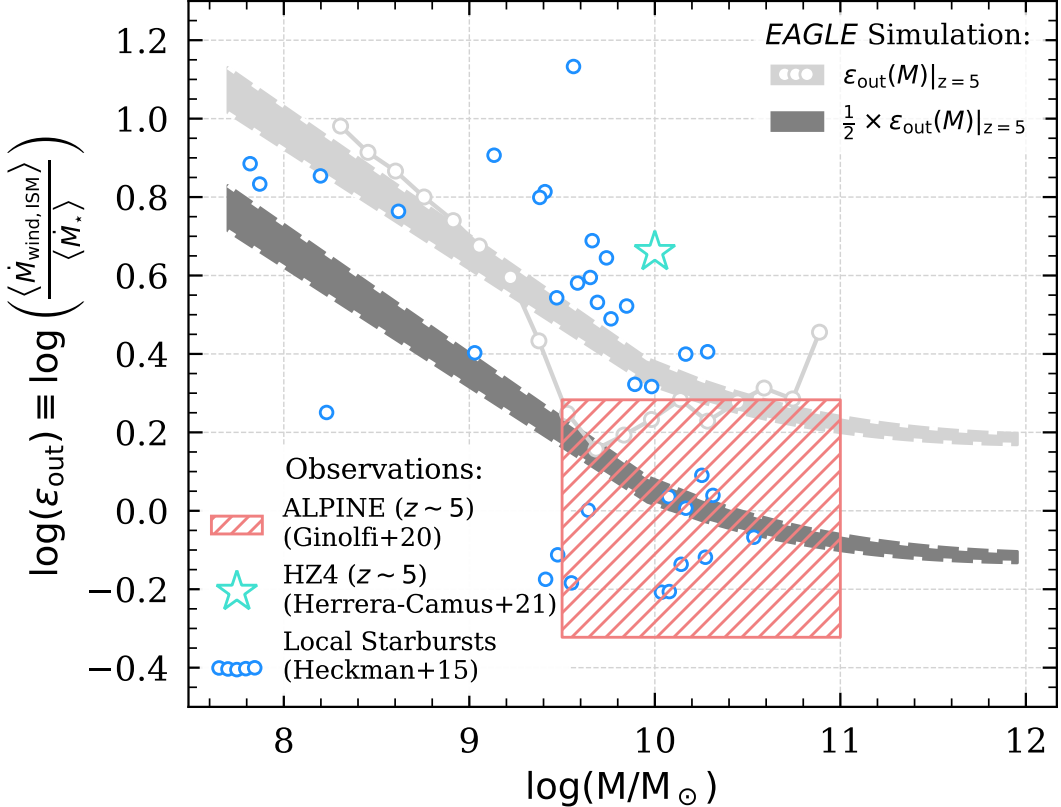


**Figure B.3.** Parameterization of the mass-loading factor  $\epsilon_{\text{out}}$  (Equation B1) derived by the EAGLE simulation (figure 3; P. D. Mitchell et al. 2020). The light gray curve show the nominal outflow efficiency from EAGLE. The dark gray curve shows a two-times reduced outflow efficiency. We compare this to observations at  $z \sim 5$  of the ALPINE sample (red hatched square; M. Ginolfi et al. 2020; J. E. Birkin et al. 2025) and HZ4 (turquoise star; R. Herrera-Camus et al. 2021), as well as local starbursts (blue circles; T. M. Heckman et al. 2015). Note that the ALPINE sample is more consistent with a reduced outflow efficiency, which is also preferred to reproduce the MZR (Figure 4).

the outflow efficiency is also preferred to reproduce the MZR of  $z \sim 5$  galaxies (Figure 4). This has also been noticed in A. Pallottini et al. (2025) and S. Carniani et al. (2024). We note that the simulated mass-loading factors may be inferred differently compared to the observations which could cause this discrepancy (e.g., E. Pizzati et al. 2020; S. Carniani et al. 2024).

## REFERENCES

Abazajian, K. N., Adelman-McCarthy, J. K., Agüeros, M. A., et al. 2009, ApJS, 182, 543, doi: [10.1088/0067-0049/182/2/543](https://doi.org/10.1088/0067-0049/182/2/543)

Alam, S., Albareti, F. D., Allende Prieto, C., et al. 2015, ApJS, 219, 12, doi: [10.1088/0067-0049/219/1/12](https://doi.org/10.1088/0067-0049/219/1/12)

Allende Prieto, C., Lambert, D. L., & Asplund, M. 2001, ApJL, 556, L63, doi: [10.1086/322874](https://doi.org/10.1086/322874)

Andrews, B. H., & Martini, P. 2013, ApJ, 765, 140, doi: [10.1088/0004-637X/765/2/140](https://doi.org/10.1088/0004-637X/765/2/140)

Arnouts, S., Cristiani, S., Moscardini, L., et al. 1999, MNRAS, 310, 540, doi: [10.1046/j.1365-8711.1999.02978.x](https://doi.org/10.1046/j.1365-8711.1999.02978.x)

Asada, Y., Sawicki, M., Abraham, R., et al. 2023, arXiv e-prints, arXiv:2310.02314, doi: [10.48550/arXiv.2310.02314](https://doi.org/10.48550/arXiv.2310.02314)

Asplund, M., Grevesse, N., Sauval, A. J., & Scott, P. 2009, ARA&A, 47, 481, doi: [10.1146/annurev.astro.46.060407.145222](https://doi.org/10.1146/annurev.astro.46.060407.145222)

Astropy Collaboration, Robitaille, T. P., Tollerud, E. J., et al. 2013, A&A, 558, A33, doi: [10.1051/0004-6361/201322068](https://doi.org/10.1051/0004-6361/201322068)

Astropy Collaboration, Price-Whelan, A. M., Sipőcz, B. M., et al. 2018, AJ, 156, 123, doi: [10.3847/1538-3881/aabc4f](https://doi.org/10.3847/1538-3881/aabc4f)

Astropy Collaboration, Price-Whelan, A. M., Lim, P. L., et al. 2022, ApJ, 935, 167, doi: [10.3847/1538-4357/ac7c74](https://doi.org/10.3847/1538-4357/ac7c74)

Baldwin, J. A., Phillips, M. M., & Terlevich, R. 1981, PASP, 93, 5, doi: [10.1086/130766](https://doi.org/10.1086/130766)

Baugh, C. M., Gonzalez-Perez, V., Lagos, C. D. P., et al. 2019, MNRAS, 483, 4922, doi: [10.1093/mnras/sty3427](https://doi.org/10.1093/mnras/sty3427)

Berg, D. A., Skillman, E. D., Marble, A. R., et al. 2012, ApJ, 754, 98, doi: [10.1088/0004-637X/754/2/98](https://doi.org/10.1088/0004-637X/754/2/98)

Bergemann, M., Hoppe, R., Semenova, E., et al. 2021, MNRAS, 508, 2236, doi: [10.1093/mnras/stab2160](https://doi.org/10.1093/mnras/stab2160)

Béthermin, M., Fudamoto, Y., Ginolfi, M., et al. 2020, A&A, 643, A2, doi: [10.1051/0004-6361/202037649](https://doi.org/10.1051/0004-6361/202037649)

Birkin, J. E., Spilker, J. S., Herrera-Camus, R., et al. 2025, ApJ, 985, 243, doi: [10.3847/1538-4357/adced3](https://doi.org/10.3847/1538-4357/adced3)

Boquien, M., Burgarella, D., Roehlly, Y., et al. 2019, A&A, 622, A103, doi: [10.1051/0004-6361/201834156](https://doi.org/10.1051/0004-6361/201834156)

Boylan-Kolchin, M., Springel, V., White, S. D. M., Jenkins, A., & Lemson, G. 2009, MNRAS, 398, 1150, doi: [10.1111/j.1365-2966.2009.15191.x](https://doi.org/10.1111/j.1365-2966.2009.15191.x)

Burgarella, D., Buat, V., & Iglesias-Páramo, J. 2005, MNRAS, 360, 1413, doi: [10.1111/j.1365-2966.2005.09131.x](https://doi.org/10.1111/j.1365-2966.2005.09131.x)

Burgarella, D., Buat, V., Theulé, P., et al. 2025, A&A, 699, A336, doi: [10.1051/0004-6361/202554231](https://doi.org/10.1051/0004-6361/202554231)

Caplar, N., & Tacchella, S. 2019, MNRAS, 487, 3845, doi: [10.1093/mnras/stz1449](https://doi.org/10.1093/mnras/stz1449)

Carniani, S., Venturi, G., Parlanti, E., et al. 2024, A&A, 685, A99, doi: [10.1051/0004-6361/202347230](https://doi.org/10.1051/0004-6361/202347230)

Casey, C. M., Kartaltepe, J. S., Drakos, N. E., et al. 2022, arXiv e-prints, arXiv:2211.07865, doi: [10.48550/arXiv.2211.07865](https://doi.org/10.48550/arXiv.2211.07865)

Chabrier, G. 2003, PASP, 115, 763, doi: [10.1086/376392](https://doi.org/10.1086/376392)

Christensen, L., Laursen, P., Richard, J., et al. 2012a, MNRAS, 427, 1973, doi: [10.1111/j.1365-2966.2012.22007.x](https://doi.org/10.1111/j.1365-2966.2012.22007.x)

Christensen, L., Richard, J., Hjorth, J., et al. 2012b, MNRAS, 427, 1953, doi: [10.1111/j.1365-2966.2012.22006.x](https://doi.org/10.1111/j.1365-2966.2012.22006.x)

Ciesla, L., Elbaz, D., Ilbert, O., et al. 2024, A&A, 686, A128, doi: [10.1051/0004-6361/202348091](https://doi.org/10.1051/0004-6361/202348091)

Connolly, S. D. 2016, DELightcurveSimulation: Light curve simulation code., Astrophysics Source Code Library, record ascl:1602.012 <http://ascl.net/1602.012>

Crain, R. A., Schaye, J., Bower, R. G., et al. 2015, MNRAS, 450, 1937, doi: [10.1093/mnras/stv725](https://doi.org/10.1093/mnras/stv725)

Cullen, F., McLure, R. J., Dunlop, J. S., et al. 2019, MNRAS, 487, 2038, doi: [10.1093/mnras/stz1402](https://doi.org/10.1093/mnras/stz1402)

Curti, M., Mannucci, F., Cresci, G., & Maiolino, R. 2020, MNRAS, 491, 944, doi: [10.1093/mnras/stz2910](https://doi.org/10.1093/mnras/stz2910)

Curti, M., D'Eugenio, F., Carniani, S., et al. 2023, MNRAS, 518, 425, doi: [10.1093/mnras/stac2737](https://doi.org/10.1093/mnras/stac2737)

Curti, M., Maiolino, R., Curtis-Lake, E., et al. 2024, A&A, 684, A75, doi: [10.1051/0004-6361/202346698](https://doi.org/10.1051/0004-6361/202346698)

Daflon, S., & Cunha, K. 2004, ApJ, 617, 1115, doi: [10.1086/425607](https://doi.org/10.1086/425607)

Davé, R., Finlator, K., & Oppenheimer, B. D. 2012, MNRAS, 421, 98, doi: [10.1111/j.1365-2966.2011.20148.x](https://doi.org/10.1111/j.1365-2966.2011.20148.x)

Davies, R. L., Förster Schreiber, N. M., Übler, H., et al. 2019, ApJ, 873, 122, doi: [10.3847/1538-4357/ab06f1](https://doi.org/10.3847/1538-4357/ab06f1)

Dayal, P., Ferrara, A., & Dunlop, J. S. 2013, MNRAS, 430, 2891, doi: [10.1093/mnras/stt083](https://doi.org/10.1093/mnras/stt083)

De Lucia, G., Fontanot, F., Xie, L., & Hirschmann, M. 2024, A&A, 687, A68, doi: [10.1051/0004-6361/202349045](https://doi.org/10.1051/0004-6361/202349045)

De Lucia, G., Tornatore, L., Frenk, C. S., et al. 2014, MNRAS, 445, 970, doi: [10.1093/mnras/stu1752](https://doi.org/10.1093/mnras/stu1752)

De Lucia, G., Xie, L., Fontanot, F., & Hirschmann, M. 2020, MNRAS, 498, 3215, doi: [10.1093/mnras/staa2556](https://doi.org/10.1093/mnras/staa2556)

Dekel, A., & Mandelker, N. 2014, MNRAS, 444, 2071, doi: [10.1093/mnras/stu1427](https://doi.org/10.1093/mnras/stu1427)

Dell'Agli, F., Valiante, R., Kamath, D., Ventura, P., & García-Hernández, D. A. 2019, MNRAS, 486, 4738, doi: [10.1093/mnras/stz1164](https://doi.org/10.1093/mnras/stz1164)

Dessauges-Zavadsky, M., Ginolfi, M., Pozzi, F., et al. 2020, A&A, 643, A5, doi: [10.1051/0004-6361/202038231](https://doi.org/10.1051/0004-6361/202038231)

Dubois, Y., Volonteri, M., & Silk, J. 2014, MNRAS, 440, 1590, doi: [10.1093/mnras/stu373](https://doi.org/10.1093/mnras/stu373)

Dubois, Y., Beckmann, R., Bournaud, F., et al. 2021, A&A, 651, A109, doi: [10.1051/0004-6361/202039429](https://doi.org/10.1051/0004-6361/202039429)

Elia, D., Molinari, S., Schisano, E., et al. 2022, ApJ, 941, 162, doi: [10.3847/1538-4357/aca27d](https://doi.org/10.3847/1538-4357/aca27d)

Ellison, S. L., Patton, D. R., Simard, L., & McConnachie, A. W. 2008, AJ, 135, 1877, doi: [10.1088/0004-6256/135/5/1877](https://doi.org/10.1088/0004-6256/135/5/1877)

Emami, N., Siana, B., Weisz, D. R., et al. 2019, ApJ, 881, 71, doi: [10.3847/1538-4357/ab211a](https://doi.org/10.3847/1538-4357/ab211a)

Emmanoulopoulos, D., McHardy, I. M., & Papadakis, I. E. 2013, MNRAS, 433, 907, doi: [10.1093/mnras/stt764](https://doi.org/10.1093/mnras/stt764)

Endsley, R., Chisholm, J., Stark, D. P., Topping, M. W., & Whitler, L. 2024, arXiv e-prints, arXiv:2410.01905, doi: [10.48550/arXiv.2410.01905](https://doi.org/10.48550/arXiv.2410.01905)

Faisst, A., X, X., & et al. 2025, submitted, ApJ

Faisst, A. L., Capak, P. L., Emami, N., Tacchella, S., & Larson, K. L. 2019, ApJ, 884, 133, doi: [10.3847/1538-4357/ab425b](https://doi.org/10.3847/1538-4357/ab425b)

Faisst, A. L., & Morishita, T. 2024, ApJ, 971, 47, doi: [10.3847/1538-4357/ad58e2](https://doi.org/10.3847/1538-4357/ad58e2)

Faisst, A. L., Schaefer, D., Lemaux, B. C., et al. 2020, ApJS, 247, 61, doi: [10.3847/1538-4365/ab7cc0](https://doi.org/10.3847/1538-4365/ab7cc0)

Faucher-Giguère, C.-A. 2018, MNRAS, 473, 3717, doi: [10.1093/mnras/stx2595](https://doi.org/10.1093/mnras/stx2595)

Faucher-Giguère, C.-A., Quataert, E., & Hopkins, P. F. 2013, MNRAS, 433, 1970, doi: [10.1093/mnras/stt866](https://doi.org/10.1093/mnras/stt866)

Feldmann, R. 2015, MNRAS, 449, 3274, doi: [10.1093/mnras/stv552](https://doi.org/10.1093/mnras/stv552)

Fontanot, F., De Lucia, G., Hirschmann, M., et al. 2020, MNRAS, 496, 3943, doi: [10.1093/mnras/staa1716](https://doi.org/10.1093/mnras/staa1716)

Fontanot, F., La Barbera, F., De Lucia, G., et al. 2024, A&A, 686, A302, doi: [10.1051/0004-6361/202348688](https://doi.org/10.1051/0004-6361/202348688)

Fujimoto, S., Faisst, A. L., & et al. 2025, in prep, ApJ

Fujimoto, S., Ouchi, M., Ferrara, A., et al. 2019, ApJ, 887, 107, doi: [10.3847/1538-4357/ab480f](https://doi.org/10.3847/1538-4357/ab480f)

Furlanetto, S. R., & Mirocha, J. 2022, MNRAS, 511, 3895, doi: [10.1093/mnras/stac310](https://doi.org/10.1093/mnras/stac310)

Garaldi, E., Kannan, R., Smith, A., et al. 2022, MNRAS, 512, 4909, doi: [10.1093/mnras/stac257](https://doi.org/10.1093/mnras/stac257)

Ginolfi, M., Jones, G. C., Béthermin, M., et al. 2020, A&A, 633, A90, doi: [10.1051/0004-6361/201936872](https://doi.org/10.1051/0004-6361/201936872)

Guo, Y., Koo, D. C., Lu, Y., et al. 2016, ApJ, 822, 103, doi: [10.3847/0004-637X/822/2/103](https://doi.org/10.3847/0004-637X/822/2/103)

Heckman, T. M., Alexandroff, R. M., Borthakur, S., Overzier, R., & Leitherer, C. 2015, ApJ, 809, 147, doi: [10.1088/0004-637X/809/2/147](https://doi.org/10.1088/0004-637X/809/2/147)

Heintz, K. E., Brammer, G. B., Watson, D., et al. 2025, A&A, 693, A60, doi: [10.1051/0004-6361/202450243](https://doi.org/10.1051/0004-6361/202450243)

Henry, A., Rafelski, M., Sunnquist, B., et al. 2021, ApJ, 919, 143, doi: [10.3847/1538-4357/ac1105](https://doi.org/10.3847/1538-4357/ac1105)

Herrera-Camus, R., Förster Schreiber, N., Genzel, R., et al. 2021, A&A, 649, A31, doi: [10.1051/0004-6361/202039704](https://doi.org/10.1051/0004-6361/202039704)

Herrera-Camus, R., González-López, J., Förster Schreiber, N., et al. 2025, arXiv e-prints, arXiv:2505.06340, doi: [10.48550/arXiv.2505.06340](https://doi.org/10.48550/arXiv.2505.06340)

Hirschmann, M., Charlot, S., & Somerville, R. S. 2023, MNRAS, 526, 3504, doi: [10.1093/mnras/stad2745](https://doi.org/10.1093/mnras/stad2745)

Hirschmann, M., De Lucia, G., & Fontanot, F. 2016, MNRAS, 461, 1760, doi: [10.1093/mnras/stw1318](https://doi.org/10.1093/mnras/stw1318)

Hopkins, P. F., Kereš, D., Oñorbe, J., et al. 2014, MNRAS, 445, 581, doi: [10.1093/mnras/stu1738](https://doi.org/10.1093/mnras/stu1738)

Hopkins, P. F., Wetzel, A., Kereš, D., et al. 2018, MNRAS, 480, 800, doi: [10.1093/mnras/sty1690](https://doi.org/10.1093/mnras/sty1690)

Hopkins, P. F., Wetzel, A., Wheeler, C., et al. 2023, MNRAS, 519, 3154, doi: [10.1093/mnras/stac3489](https://doi.org/10.1093/mnras/stac3489)

Ilbert, O., Arnouts, S., McCracken, H. J., et al. 2006, A&A, 457, 841, doi: [10.1051/0004-6361:20065138](https://doi.org/10.1051/0004-6361:20065138)

Kannan, R., Garaldi, E., Smith, A., et al. 2022, MNRAS, 511, 4005, doi: [10.1093/mnras/stab3710](https://doi.org/10.1093/mnras/stab3710)

Kannan, R., Marinacci, F., Vogelsberger, M., et al. 2020, MNRAS, 499, 5732, doi: [10.1093/mnras/staa3249](https://doi.org/10.1093/mnras/staa3249)

Kannan, R., Vogelsberger, M., Marinacci, F., et al. 2021, MNRAS, 503, 336, doi: [10.1093/mnras/stab416](https://doi.org/10.1093/mnras/stab416)

Kannan, R., Puchwein, E., Smith, A., et al. 2025, arXiv e-prints, arXiv:2502.20437, doi: [10.48550/arXiv.2502.20437](https://doi.org/10.48550/arXiv.2502.20437)

Kashino, D., Silverman, J. D., Rodighiero, G., et al. 2013, ApJL, 777, L8, doi: [10.1088/2041-8205/777/1/L8](https://doi.org/10.1088/2041-8205/777/1/L8)

Kashino, D., Silverman, J. D., Sanders, D., et al. 2017, ApJ, 835, 88, doi: [10.3847/1538-4357/835/1/88](https://doi.org/10.3847/1538-4357/835/1/88)

Katz, H., Liu, S., Kimm, T., et al. 2022, arXiv e-prints, arXiv:2211.04626, doi: [10.48550/arXiv.2211.04626](https://doi.org/10.48550/arXiv.2211.04626)

Katz, H., Rosdahl, J., Kimm, T., et al. 2023, arXiv e-prints, arXiv:2309.03269, doi: [10.48550/arXiv.2309.03269](https://doi.org/10.48550/arXiv.2309.03269)

Kennicutt, Robert C., J. 1998, ApJ, 498, 541, doi: [10.1086/305588](https://doi.org/10.1086/305588)

Kewley, L. J., Nicholls, D. C., & Sutherland, R. S. 2019, ARA&A, 57, 511, doi: [10.1146/annurev-astro-081817-051832](https://doi.org/10.1146/annurev-astro-081817-051832)

Khusanova, Y., Béthermin, M., Le Fèvre, O., et al. 2021, A&A, 649, A152, doi: [10.1051/0004-6361/202038944](https://doi.org/10.1051/0004-6361/202038944)

Koekemoer, A. M., Aussel, H., Calzetti, D., et al. 2007, ApJS, 172, 196, doi: [10.1086/520086](https://doi.org/10.1086/520086)

Korhonen Cuestas, N. A., Strom, A. L., Miller, T. B., et al. 2025, arXiv e-prints, arXiv:2503.10800, doi: [10.48550/arXiv.2503.10800](https://doi.org/10.48550/arXiv.2503.10800)

Kriek, M., Shapley, A. E., Reddy, N. A., et al. 2015, ApJS, 218, 15, doi: [10.1088/0067-0049/218/2/15](https://doi.org/10.1088/0067-0049/218/2/15)

Krumholz, M. R., & Dekel, A. 2012, ApJ, 753, 16, doi: [10.1088/0004-637X/753/1/16](https://doi.org/10.1088/0004-637X/753/1/16)

Lapi, A., Mancuso, C., Celotti, A., & Danese, L. 2017, ApJ, 835, 37, doi: [10.3847/1538-4357/835/1/37](https://doi.org/10.3847/1538-4357/835/1/37)

Lapi, A., Pantoni, L., Boco, L., & Danese, L. 2020, ApJ, 897, 81, doi: [10.3847/1538-4357/ab9812](https://doi.org/10.3847/1538-4357/ab9812)

Lara-López, M. A., Cepa, J., Bongiovanni, A., et al. 2010, A&A, 521, L53, doi: [10.1051/0004-6361/201014803](https://doi.org/10.1051/0004-6361/201014803)

Le Fèvre, O., Béthermin, M., Faisst, A., et al. 2020, A&A, 643, A1, doi: [10.1051/0004-6361/201936965](https://doi.org/10.1051/0004-6361/201936965)

Licquia, T. C., & Newman, J. A. 2015, ApJ, 806, 96, doi: [10.1088/0004-637X/806/1/96](https://doi.org/10.1088/0004-637X/806/1/96)

Lilly, S. J., Carollo, C. M., Pipino, A., Renzini, A., & Peng, Y. 2013, ApJ, 772, 119, doi: [10.1088/0004-637X/772/2/119](https://doi.org/10.1088/0004-637X/772/2/119)

Limongi, M., & Chieffi, A. 2018, ApJS, 237, 13, doi: [10.3847/1538-4365/aacb24](https://doi.org/10.3847/1538-4365/aacb24)

Liu, L.-J., Faisst, A., & et al. 2025, in prep, ApJ

Liu, L.-J., Sun, G., Chang, T.-C., Furlanetto, S. R., & Bradford, C. M. 2024, ApJ, 974, 175, doi: [10.3847/1538-4357/ad73d5](https://doi.org/10.3847/1538-4357/ad73d5)

Lopez, F., X, X., & et al. 2025, in prep, ApJ

Luridiana, V., Morisset, C., & Shaw, R. A. 2015, A&A, 573, A42, doi: [10.1051/0004-6361/201323152](https://doi.org/10.1051/0004-6361/201323152)

Ma, X., Hopkins, P. F., Faucher-Giguère, C.-A., et al. 2016, *MNRAS*, 456, 2140, doi: [10.1093/mnras/stv2659](https://doi.org/10.1093/mnras/stv2659)

Ma, X., Hopkins, P. F., Boylan-Kolchin, M., et al. 2018a, *MNRAS*, 477, 219, doi: [10.1093/mnras/sty684](https://doi.org/10.1093/mnras/sty684)

Ma, X., Hopkins, P. F., Garrison-Kimmel, S., et al. 2018b, *MNRAS*, 478, 1694, doi: [10.1093/mnras/sty1024](https://doi.org/10.1093/mnras/sty1024)

Ma, X., Hayward, C. C., Casey, C. M., et al. 2019, *MNRAS*, 487, 1844, doi: [10.1093/mnras/stz1324](https://doi.org/10.1093/mnras/stz1324)

Maier, C., Lilly, S. J., Ziegler, B. L., et al. 2014, *ApJ*, 792, 3, doi: [10.1088/0004-637X/792/1/3](https://doi.org/10.1088/0004-637X/792/1/3)

Maiolino, R., & Mannucci, F. 2019, *A&A Rv*, 27, 3, doi: [10.1007/s00159-018-0112-2](https://doi.org/10.1007/s00159-018-0112-2)

Maiolino, R., Nagao, T., Grazian, A., et al. 2008, *A&A*, 488, 463, doi: [10.1051/0004-6361:200809678](https://doi.org/10.1051/0004-6361:200809678)

Mannucci, F., Cresci, G., Maiolino, R., Marconi, A., & Gnerucci, A. 2010, *MNRAS*, 408, 2115, doi: [10.1111/j.1365-2966.2010.17291.x](https://doi.org/10.1111/j.1365-2966.2010.17291.x)

Marinacci, F., Sales, L. V., Vogelsberger, M., Torrey, P., & Springel, V. 2019, *MNRAS*, 489, 4233, doi: [10.1093/mnras/stz2391](https://doi.org/10.1093/mnras/stz2391)

Marinacci, F., Vogelsberger, M., Pakmor, R., et al. 2018, *MNRAS*, 480, 5113, doi: [10.1093/mnras/sty2206](https://doi.org/10.1093/mnras/sty2206)

Marszewski, A., Sun, G., Faucher-Giguère, C.-A., Hayward, C. C., & Feldmann, R. 2024, *ApJL*, 967, L41, doi: [10.3847/2041-8213/ad4cee](https://doi.org/10.3847/2041-8213/ad4cee)

Mehta, V., Teplitz, H. I., Scarlata, C., et al. 2023, *ApJ*, 952, 133, doi: [10.3847/1538-4357/acd9cf](https://doi.org/10.3847/1538-4357/acd9cf)

Mitchell, P. D., Schaye, J., Bower, R. G., & Crain, R. A. 2020, *MNRAS*, 494, 3971, doi: [10.1093/mnras/staa938](https://doi.org/10.1093/mnras/staa938)

Mitsuhashi, I., Tadaki, K.-i., Ikeda, R., et al. 2024, *A&A*, 690, A197, doi: [10.1051/0004-6361/202348782](https://doi.org/10.1051/0004-6361/202348782)

Mollá, M., Díaz, Á. I., Cavichia, O., et al. 2019, *MNRAS*, 482, 3071, doi: [10.1093/mnras/sty2877](https://doi.org/10.1093/mnras/sty2877)

Morishita, T., Liu, Z., Stiavelli, M., et al. 2025, arXiv e-prints, arXiv:2507.10521, doi: [10.48550/arXiv.2507.10521](https://doi.org/10.48550/arXiv.2507.10521)

Morishita, T., Stiavelli, M., Grillo, C., et al. 2024, *ApJ*, 971, 43, doi: [10.3847/1538-4357/ad5290](https://doi.org/10.3847/1538-4357/ad5290)

Muñoz, J. B., Mirocha, J., Furlanetto, S., & Sabti, N. 2023, *MNRAS*, 526, L47, doi: [10.1093/mnrasl/slad115](https://doi.org/10.1093/mnrasl/slad115)

Muratov, A. L., Kereš, D., Faucher-Giguère, C.-A., et al. 2015, *MNRAS*, 454, 2691, doi: [10.1093/mnras/stv2126](https://doi.org/10.1093/mnras/stv2126)

Nagao, T., Maiolino, R., & Marconi, A. 2006, *A&A*, 459, 85, doi: [10.1051/0004-6361:20065216](https://doi.org/10.1051/0004-6361:20065216)

Naiman, J. P., Pillepich, A., Springel, V., et al. 2018, *MNRAS*, 477, 1206, doi: [10.1093/mnras/sty618](https://doi.org/10.1093/mnras/sty618)

Nakajima, K., Ouchi, M., Isobe, Y., et al. 2023, *ApJS*, 269, 33, doi: [10.3847/1538-4365/acd556](https://doi.org/10.3847/1538-4365/acd556)

Navarro-Carrera, R., Rinaldi, P., Caputi, K. I., et al. 2024, arXiv e-prints, arXiv:2410.23249, doi: [10.48550/arXiv.2410.23249](https://doi.org/10.48550/arXiv.2410.23249)

Nelson, D., Pillepich, A., Springel, V., et al. 2018, *MNRAS*, 475, 624, doi: [10.1093/mnras/stx3040](https://doi.org/10.1093/mnras/stx3040)

Nelson, D., Pillepich, A., Springel, V., et al. 2019, *MNRAS*, 490, 3234, doi: [10.1093/mnras/stz2306](https://doi.org/10.1093/mnras/stz2306)

Oke, J. B. 1974, *ApJS*, 27, 21, doi: [10.1086/190287](https://doi.org/10.1086/190287)

Onodera, M., Carollo, C. M., Lilly, S., et al. 2016, *ApJ*, 822, 42, doi: [10.3847/0004-637X/822/1/42](https://doi.org/10.3847/0004-637X/822/1/42)

Osman, O., X, X., & et al. 2025, in prep, *ApJ*

Pagel, B. E. J. 1997, *Nucleosynthesis and Chemical Evolution of Galaxies*

Pallottini, A., Ferrara, A., Gallerani, S., et al. 2025, *A&A*, 699, A6, doi: [10.1051/0004-6361/202451742](https://doi.org/10.1051/0004-6361/202451742)

Pallottini, A., Ferrara, A., Gallerani, S., et al. 2022, *MNRAS*, 513, 5621, doi: [10.1093/mnras/stac1281](https://doi.org/10.1093/mnras/stac1281)

Pantoni, L., Lapi, A., Massardi, M., Goswami, S., & Danese, L. 2019, *ApJ*, 880, 129, doi: [10.3847/1538-4357/ab2adc](https://doi.org/10.3847/1538-4357/ab2adc)

Papovich, C., Simons, R. C., Estrada-Carpenter, V., et al. 2022, *ApJ*, 937, 22, doi: [10.3847/1538-4357/ac8058](https://doi.org/10.3847/1538-4357/ac8058)

Pérez-Montero, E., Contini, T., Lamareille, F., et al. 2013, *A&A*, 549, A25, doi: [10.1051/0004-6361/201220070](https://doi.org/10.1051/0004-6361/201220070)

Péroux, C., & Howk, J. C. 2020, *ARA&A*, 58, 363, doi: [10.1146/annurev-astro-021820-120014](https://doi.org/10.1146/annurev-astro-021820-120014)

Pettini, M., & Pagel, B. E. J. 2004, *MNRAS*, 348, L59, doi: [10.1111/j.1365-2966.2004.07591.x](https://doi.org/10.1111/j.1365-2966.2004.07591.x)

Pillepich, A., Nelson, D., Hernquist, L., et al. 2018, *MNRAS*, 475, 648, doi: [10.1093/mnras/stx3112](https://doi.org/10.1093/mnras/stx3112)

Pillepich, A., Nelson, D., Springel, V., et al. 2019, *MNRAS*, 490, 3196, doi: [10.1093/mnras/stz2338](https://doi.org/10.1093/mnras/stz2338)

Pilyugin, L. S., Thuan, T. X., & Vílchez, J. M. 2006, *MNRAS*, 367, 1139, doi: [10.1111/j.1365-2966.2006.10033.x](https://doi.org/10.1111/j.1365-2966.2006.10033.x)

Pizzati, E., Ferrara, A., Pallottini, A., et al. 2020, *MNRAS*, 495, 160, doi: [10.1093/mnras/staa1163](https://doi.org/10.1093/mnras/staa1163)

Planck Collaboration, Ade, P. A. R., Aghanim, N., et al. 2014, *A&A*, 571, A16, doi: [10.1051/0004-6361/201321591](https://doi.org/10.1051/0004-6361/201321591)

Portinari, L., Chiosi, C., & Bressan, A. 1998, *A&A*, 334, 505, doi: [10.48550/arXiv.astro-ph/9711337](https://doi.org/10.48550/arXiv.astro-ph/9711337)

Ren, W., Silverman, J., & et al. 2025, submitted, *ApJ*

Rosdahl, J., Katz, H., Blaizot, J., et al. 2018, *MNRAS*, 479, 994, doi: [10.1093/mnras/sty1655](https://doi.org/10.1093/mnras/sty1655)

Rosdahl, J., Blaizot, J., Katz, H., et al. 2022, *MNRAS*, 515, 2386, doi: [10.1093/mnras/stac1942](https://doi.org/10.1093/mnras/stac1942)

Rowland, L. E., Stefanon, M., Bouwens, R., et al. 2025, arXiv e-prints, arXiv:2501.10559, doi: [10.48550/arXiv.2501.10559](https://doi.org/10.48550/arXiv.2501.10559)

Rudie, G. C., Steidel, C. C., Trainor, R. F., et al. 2012, *ApJ*, 750, 67, doi: [10.1088/0004-637X/750/1/67](https://doi.org/10.1088/0004-637X/750/1/67)

Salim, S., Lee, J. C., Davé, R., & Dickinson, M. 2015, *ApJ*, 808, 25, doi: [10.1088/0004-637X/808/1/25](https://doi.org/10.1088/0004-637X/808/1/25)

Sánchez, S. F., Barrera-Ballesteros, J. K., Sánchez-Menguiano, L., et al. 2017, *MNRAS*, 469, 2121, doi: [10.1093/mnras/stx808](https://doi.org/10.1093/mnras/stx808)

Sánchez Almeida, J., Morales-Luis, A. B., Muñoz-Tuñón, C., et al. 2014, *ApJ*, 783, 45, doi: [10.1088/0004-637X/783/1/45](https://doi.org/10.1088/0004-637X/783/1/45)

Sánchez Almeida, J., Elmegreen, B. G., Muñoz-Tuñón, C., et al. 2015, *ApJL*, 810, L15, doi: [10.1088/2041-8205/810/2/L15](https://doi.org/10.1088/2041-8205/810/2/L15)

Sanders, R. L., Shapley, A. E., Topping, M. W., Reddy, N. A., & Brammer, G. B. 2024, *ApJ*, 962, 24, doi: [10.3847/1538-4357/ad15fc](https://doi.org/10.3847/1538-4357/ad15fc)

Sanders, R. L., Shapley, A. E., Kriek, M., et al. 2015, *ApJ*, 799, 138, doi: [10.1088/0004-637X/799/2/138](https://doi.org/10.1088/0004-637X/799/2/138)

Sanders, R. L., Shapley, A. E., Kriek, M., et al. 2018, *ApJ*, 858, 99, doi: [10.3847/1538-4357/aabcb](https://doi.org/10.3847/1538-4357/aabcb)

Sanders, R. L., Shapley, A. E., Jones, T., et al. 2021, *ApJ*, 914, 19, doi: [10.3847/1538-4357/abf4c1](https://doi.org/10.3847/1538-4357/abf4c1)

Sarkar, A., Chakraborty, P., Vogelsberger, M., et al. 2025, *ApJ*, 978, 136, doi: [10.3847/1538-4357/ad8f32](https://doi.org/10.3847/1538-4357/ad8f32)

Schaye, J., Crain, R. A., Bower, R. G., et al. 2015, *MNRAS*, 446, 521, doi: [10.1093/mnras/stu2058](https://doi.org/10.1093/mnras/stu2058)

Scoville, N., Aussel, H., Brusa, M., et al. 2007, *ApJS*, 172, 1, doi: [10.1086/516585](https://doi.org/10.1086/516585)

Scoville, N., Faisst, A., Weaver, J., et al. 2023, *ApJ*, 943, 82, doi: [10.3847/1538-4357/aca1bc](https://doi.org/10.3847/1538-4357/aca1bc)

Shen, X., Vogelsberger, M., Boylan-Kolchin, M., Tacchella, S., & Kannan, R. 2023, *MNRAS*, 525, 3254, doi: [10.1093/mnras/stad2508](https://doi.org/10.1093/mnras/stad2508)

Shutov, M., Ilbert, O., Toft, S., et al. 2025, *A&A*, 695, A20, doi: [10.1051/0004-6361/202452570](https://doi.org/10.1051/0004-6361/202452570)

Silverman, J. D., Daddi, E., Rodighiero, G., et al. 2015, *ApJL*, 812, L23, doi: [10.1088/2041-8205/812/2/L23](https://doi.org/10.1088/2041-8205/812/2/L23)

Smith, A., Kannan, R., Garaldi, E., et al. 2022, *MNRAS*, 512, 3243, doi: [10.1093/mnras/stac713](https://doi.org/10.1093/mnras/stac713)

Springel, V., White, S. D. M., Jenkins, A., et al. 2005, *Nature*, 435, 629, doi: [10.1038/nature03597](https://doi.org/10.1038/nature03597)

Springel, V., Pakmor, R., Pillepich, A., et al. 2018, *MNRAS*, 475, 676, doi: [10.1093/mnras/stx3304](https://doi.org/10.1093/mnras/stx3304)

Steidel, C. C., Rudie, G. C., Strom, A. L., et al. 2014, *ApJ*, 795, 165, doi: [10.1088/0004-637X/795/2/165](https://doi.org/10.1088/0004-637X/795/2/165)

Strom, A. L., Rudie, G. C., Steidel, C. C., & Trainor, R. F. 2022, *ApJ*, 925, 116, doi: [10.3847/1538-4357/ac38a3](https://doi.org/10.3847/1538-4357/ac38a3)

Strom, A. L., Steidel, C. C., Rudie, G. C., et al. 2017, *ApJ*, 836, 164, doi: [10.3847/1538-4357/836/2/164](https://doi.org/10.3847/1538-4357/836/2/164)

Sun, G., Muñoz, J. B., Mirocha, J., & Faucher-Giguère, C.-A. 2025, *JCAP*, 2025, 034, doi: [10.1088/1475-7516/2025/04/034](https://doi.org/10.1088/1475-7516/2025/04/034)

Tinsley, B. M. 1980, *FCPh*, 5, 287, doi: [10.48550/arXiv.2203.02041](https://doi.org/10.48550/arXiv.2203.02041)

Topping, M. W., Shapley, A. E., Sanders, R. L., et al. 2021, *MNRAS*, 506, 1237, doi: [10.1093/mnras/stab1793](https://doi.org/10.1093/mnras/stab1793)

Topping, M. W., Sanders, R. L., Shapley, A. E., et al. 2025, *MNRAS*, 541, 1707, doi: [10.1093/mnras/staf903](https://doi.org/10.1093/mnras/staf903)

Tremonti, C. A., Heckman, T. M., Kauffmann, G., et al. 2004, *ApJ*, 613, 898, doi: [10.1086/423264](https://doi.org/10.1086/423264)

Tsujita, A., Fujimoto, S., & et al. 2025, in prep, *ApJ*

Vanzella, E., Loiacono, F., Bergamini, P., et al. 2023, *A&A*, 678, A173, doi: [10.1051/0004-6361/202346981](https://doi.org/10.1051/0004-6361/202346981)

Wang, W., Faisst, A., & et al. 2025, in prep, *ApJ*

Weisz, D. R., Johnson, B. D., Johnson, L. C., et al. 2012, *ApJ*, 744, 44, doi: [10.1088/0004-637X/744/1/44](https://doi.org/10.1088/0004-637X/744/1/44)

Welch, B., Rivera-Thorsen, T. E., Rigby, J. R., et al. 2025, *ApJ*, 980, 33, doi: [10.3847/1538-4357/ada76c](https://doi.org/10.3847/1538-4357/ada76c)

Wuyts, E., Kurk, J., Förster Schreiber, N. M., et al. 2014, *ApJL*, 789, L40, doi: [10.1088/2041-8205/789/2/L40](https://doi.org/10.1088/2041-8205/789/2/L40)

Xie, L., De Lucia, G., Hirschmann, M., & Fontanot, F. 2020, *MNRAS*, 498, 4327, doi: [10.1093/mnras/staa2370](https://doi.org/10.1093/mnras/staa2370)

Yabe, K., Ohta, K., Iwamuro, F., et al. 2014, *MNRAS*, 437, 3647, doi: [10.1093/mnras/stt2185](https://doi.org/10.1093/mnras/stt2185)

Yang, S., Lidz, A., Li, H., et al. 2025, arXiv e-prints, arXiv:2504.18006, doi: [10.48550/arXiv.2504.18006](https://doi.org/10.48550/arXiv.2504.18006)

Zahid, H. J., Dima, G. I., Kudritzki, R.-P., et al. 2014a, *ApJ*, 791, 130, doi: [10.1088/0004-637X/791/2/130](https://doi.org/10.1088/0004-637X/791/2/130)

Zahid, H. J., Kashino, D., Silverman, J. D., et al. 2014b, *ApJ*, 792, 75, doi: [10.1088/0004-637X/792/1/75](https://doi.org/10.1088/0004-637X/792/1/75)

## All Authors and Affiliations

ANDREAS L. FAISST <sup>1</sup> LUN-JUN LIU <sup>2</sup> YOHAN DUBOIS <sup>3</sup> OMIMA OSMAN <sup>4,5</sup> ANDREA PALLOTTINI <sup>6</sup>  
LIVIA VALLINI <sup>7</sup> SEIJI FUJIMOTO <sup>8,9</sup> BAHRAM MOBASHER <sup>10</sup> WUJI WANG <sup>1</sup> YU-HENG LIN <sup>1</sup>  
RICARDO O. AMORÍN <sup>11,12</sup> MANUEL ARAVENA <sup>13,14</sup> R. J. ASSEF <sup>13</sup> ANDREW J. BATTISTI <sup>15,16,17</sup>  
MATTHIEU BÉTHERMIN <sup>18</sup> MÉDÉRIC BOQUIEN <sup>19</sup> PAOLO CASSATA <sup>20,21</sup> ELISABETE DA CUNHA <sup>15,17</sup>  
POULOMI DAM <sup>20</sup> GABRIELLA DE LUCIA <sup>4,22</sup> ILSE DE LOOZE <sup>23</sup> MIROSLAVA DESSAUGES-ZAVADSKY <sup>24</sup>  
ANDREA FERRARA <sup>25</sup> KYLE FINNER <sup>1</sup> FABIO FONTANOT <sup>4,22</sup> MICHELE GINOLFI <sup>26,27</sup>  
DIEGO A. GÓMEZ-ESPINOSA <sup>28</sup> CARLOTTA GRUPPIONI <sup>7</sup> NICOL GUTIÉRREZ-VERA <sup>29,14</sup> ALI HADI <sup>10</sup>  
RODRIGO HERRERA-CAMUS <sup>29,14</sup> MICHAELA HIRSCHMANN <sup>30</sup> EDUARDO IBAR <sup>28,14</sup> HANAE INAMI <sup>31</sup>  
JEYHAN S. KARTALTEPE <sup>32</sup> ANTON M. KOEKEMOER <sup>33</sup> MAHSA KOHANDEL <sup>25</sup> LILIAN L. LEE <sup>34</sup> YUAN LI <sup>35</sup>  
JUAN MOLINA <sup>28,14</sup> AMBRA NANNI <sup>36,37</sup> DESIKA NARAYANAN <sup>38,39</sup> FRANCESCA POZZI <sup>40,7</sup>  
MONICA RELANO <sup>41,42</sup> MICHAEL ROMANO <sup>43,21</sup> DAVID B. SANDERS <sup>44</sup> JOHN D. SILVERMAN <sup>45,46,47,48</sup>  
LAURA SOMMOVIGO <sup>49</sup> JUSTIN SPILKER <sup>35</sup> AKIYOSHI TSUJITA <sup>50</sup> HANNAH ÜBLER <sup>34</sup>  
KEERTHI VASAN G.C. <sup>51</sup> ENRICO VERALDI <sup>52</sup> VINCENTE VILLANUEVA <sup>29</sup> LIZHI XIE <sup>53</sup>  
AND GIANNI ZAMORANI 

(AFFILIATIONS CAN BE FOUND AFTER THE REFERENCES)

<sup>1</sup>IPAC, California Institute of Technology, 1200 E. California Blvd. Pasadena, CA 91125, USA

<sup>2</sup>Physics Department, California Institute of Technology, 1200 E California Blvd, Pasadena, CA 91125, USA

<sup>3</sup>Institut d'Astrophysique de Paris, UMR 7095, CNRS, Sorbonne Université, 98 bis boulevard Arago, 75014 Paris, France

<sup>4</sup>INAF - Astronomical Observatory of Trieste, via G.B. Tiepolo 11, I-34143 Trieste, Italy

<sup>5</sup>University of Khartoum - Department of Physics, Al-Gamaa Ave, 11115 Khartoum, Sudan

<sup>6</sup>Dipartimento di Fisica "Enrico Fermi", Università di Pisa, Largo Bruno Pontecorvo 3, Pisa I-56127, Italy

<sup>7</sup>INAF - Osservatorio di Astrofisica e Scienza dello Spazio di Bologna, Via Gobetti 93/3, 40129 Bologna, Italy

<sup>8</sup>Department of Astronomy, The University of Texas at Austin, Austin, TX 78712, USA

<sup>9</sup>David A. Dunlap Department of Astronomy and Astrophysics, University of Toronto, 50 St. George Street, Toronto, Ontario, M5S 3H4, Canada

<sup>10</sup>Department of Physics and Astronomy, University of California, Riverside, 900 University Avenue, Riverside, CA 92521, USA

<sup>11</sup>Instituto de Investigaciòn Multidisciplinar en Ciencia y Tecnología, Universidad de La Serena, Raúl Bittrán 1305, La Serena, Chile

<sup>12</sup>Departamento de Astronomía, Universidad de La Serena, Av. Juan Cisternas 1200 Norte, La Serena, Chile

<sup>13</sup>Instituto de Estudios Astrofísicos, Facultad de Ingeniería y Ciencias, Universidad Diego Portales, Av. Ejército Libertador 441, Santiago 8370191, Chile

<sup>14</sup>Millenium Nucleus for Galaxies (MINGAL), Av. Ejército 441, Santiago 8370191, Chile

<sup>15</sup>International Centre for Radio Astronomy Research (ICRAR), The University of Western Australia, M468, 35 Stirling Highway, Crawley, WA 6009, Australia

<sup>16</sup>Research School of Astronomy and Astrophysics, Australian National University, Cotter Road, Weston Creek, ACT 2611, Australia

<sup>17</sup>ARC Center of Excellence for All Sky Astrophysics in 3 Dimensions (ASTRO 3D), Australia

<sup>18</sup>Université de Strasbourg, CNRS, Observatoire astronomique de Strasbourg, UMR 7550, 67000 Strasbourg, France

<sup>19</sup>Université Côte d'Azur, Observatoire de la Côte d'Azur, CNRS, Laboratoire Lagrange, 06000, Nice, France

<sup>20</sup>Dipartimento di Fisica e Astronomia Galileo Galilei Università degli Studi di Padova, Vicoletto dell'Osservatorio 3, 35122 Padova Italy

<sup>21</sup>INAF - Osservatorio Astronomico di Padova, Vicoletto dell'Osservatorio 5, I-35122, Padova, Italy

<sup>22</sup>IFPU - Institute for Fundamental Physics of the Universe, via Beirut 2, 34151, Trieste, Italy

<sup>23</sup>Sterrenkundig Observatorium, Ghent University, Krijgslaan 281 - S9, B-9000 Gent, Belgium

<sup>24</sup>Observatoire de Genève, Université de Genève, Chemin Pegasi 51, 1290 Versoix, Switzerland

<sup>25</sup>Scuola Normale Superiore, Piazza dei Cavalieri 7, I-56126 Pisa, Italy

<sup>26</sup>Università di Firenze, Dipartimento di Fisica e Astronomia, via G. Sansone 1, 50019 Sesto Fiorentino, Florence, Italy

<sup>27</sup>INAF — Arcetri Astrophysical Observatory, Largo E. Fermi 5, I-50125, Florence, Italy

<sup>28</sup>Instituto de Física y Astronomía, Universidad de Valparaíso, Avda. Gran Bretaña 1111, Valparaíso, Chile

<sup>29</sup>Departamento de Astronomía, Universidad de Concepción, Barrio Universitario, Concepción, Chile

<sup>30</sup>Institute of Physics, Laboratory for galaxy evolution, EPFL, Observatoire de Sauverny, Chemin Pegasi 51, 1290 Versoix, Switzerland

<sup>31</sup>Hiroshima Astrophysical Science Center, Hiroshima University, 1-3-1 Kagamiyama, Higashi-Hiroshima, Hiroshima 739-8526, Japan

<sup>32</sup>Laboratory for Multiwavelength Astrophysics, School of Physics and Astronomy, Rochester Institute of Technology, 84 Lomb Memorial Drive, Rochester, NY 14623, USA

<sup>33</sup>Space Telescope Science Institute, 3700 San Martin Dr., Baltimore, MD 21218, USA

<sup>34</sup>Max-Planck-Institute für extraterrane Physik, Giessenbachstrasse 1, 85748 Garching, Germany

<sup>35</sup>Department of Physics and Astronomy and George P. and Cynthia Woods Mitchell Institute for Fundamental Physics and Astronomy, Texas A&M University, 4242

<sup>36</sup>National Centre for Nuclear Research, ul. Pasteura 7, 02-093 Warsaw, Poland

<sup>37</sup>INAF - Osservatorio astronomico d'Abruzzo, Via Maggini SNC, 64100, Teramo, Italy

<sup>38</sup>Department of Astronomy, University of Florida, 211 Bryant Space Sciences Center, Gainesville, FL 32611, USA

<sup>39</sup>Cosmic Dawn Center (DAWN), Copenhagen, Denmark

<sup>40</sup>Dipartimento di Fisica e Astronomia "Augusto Righi", Alma Mater Studiorum, Università di Bologna, Via Gobetti 93/2, 40129 Bologna, Italy

<sup>41</sup>Dept. Física Teórica y del Cosmos, Campus de Fuentenueva, Edificio Mecenas, Universidad de Granada, E-18071, Granada, Spain

<sup>42</sup>Instituto Universitario Carlos I de Física Teórica y Computacional, Universidad de Granada, 18071, Granada, Spain

<sup>43</sup>Max-Planck-Institut für Radioastronomie, Auf dem Hügel 69, 53121 Bonn, Germany

<sup>44</sup>Institute for Astronomy, University of Hawaii, 2680 Woodlawn Drive, Honolulu, HI 96822, USA

<sup>45</sup>Kavli Institute for the Physics and Mathematics of the Universe (Kavli IPMU, WPI), UTIAS, Tokyo Institutes for Advanced Study, University of Tokyo, Chiba, 277-8583, Japan

<sup>46</sup>Department of Astronomy, Graduate School of Science, The University of Tokyo, 7-3-1 Hongo, Bunkyo, Tokyo 113-0033, Japan

<sup>47</sup>Center for Data-Driven Discovery, Kavli IPMU (WPI), UTIAS, The University of Tokyo, Kashiwa, Chiba 277-8583, Japan

<sup>48</sup>Center for Astrophysical Sciences, Department of Physics & Astronomy, Johns Hopkins University, Baltimore, MD 21218, USA

<sup>49</sup>Center for Computational Astrophysics, Flatiron Institute, 162 5th Avenue, New York, NY 10010, USA

<sup>50</sup>Institute of Astronomy, Graduate School of Science, The University of Tokyo, 2-21-1 Osawa, Mitaka, Tokyo 181-0015, Japan

<sup>51</sup>The Observatories of the Carnegie Institution for Science, 813 Santa Barbara Street, Pasadena, CA 91101, USA

<sup>52</sup>Scuola Internazionale Superiore Studi Avanzati (SISSA), Physics Area, Via Bonomea 265, 34136 Trieste, Italy

<sup>53</sup>Tianjin Normal University, Binshuixidao 393, 300387, Tianjin, China